CHARACTERIZATION OF INFRARED METASURFACE OPTICS WITH AN OPTICAL SCATTEROMETER

THESIS
Matthew R. Miller

AFIT-ENP-MS-21-D-021

DEPARTMENT OF THE AIR FORCE
AIR UNIVERSITY

AIR FORCE INSTITUTE OF TECHNOLOGY

Wright-Patterson Air Force Base, Ohio

AFIT-ENP-MS-21-D-021

CHARACTERIZATION OF INFRARED METASURFACE OPTICS WITH AN OPTICAL SCATTEROMETER

THESIS

Presented to the Faculty

Department of Engineering Physics

Graduate School of Engineering and Management

Air Force Institute of Technology

Air University

Air Education and Training Command

In Partial Fulfillment of the Requirements for the

Degree of Master of Science in Optical Sciences and Engineering

Matthew R. Miller, BS

Civilian Contractor

December 2021

AFIT-ENP-MS-21-D-021

CHARACTERIZATION OF INFRARED METASURFACE OPTICS WITH AN OPTICAL SCATTEROMETER

Matthew R. Miller, BS

Contractor

Committee Membership:

Dr. Michael Marciniak
Chair

Dr. Augustine Urbas
Member

Lt. Col. Samuel Butler, PhD
Member

Abstract

Optical metasurfaces have undergone substantial development over the last decade, and are starting to be implemented into their own scientific instruments. It is expected that they will become the preferred lenses when weight and thickness are a concern in the coming years. With this in mind, it becomes increasingly important to accurately characterize metasurface lenses and to improve on their designs. Optical scattering is one metric that is often overlooked when characterizing metasurfaces, and this thesis addresses that. An optical scatterometer is used in this experiment to create scatter profiles for one particular metasurface lens and two variants of the same design. This particular design uses dielectric pillars of varying radius to create the parabolic phase delay required for lensing. The two variants of this design change the height of the cylindrical pillars from the design height of 4.0 μm to 0.9 and 5.2 μm. Optical scatter measurements were conducted at the design wavelength of 4 μm and at 3.39 μm and 5 μm, away from design.

The results of these measurements show that when only a portion of these metasurface lenses are irradiated away from the center of the lens, they behave like blazed diffraction gratings. Where a conventional lens would show a single focal area, a diffraction grating shows multiple diffraction orders, and blazed gratings show preference to (more power within) one particular, non-zero order. The metasurface lenses show diffraction orders with a preference to the positive order direction, but also show a scatter floor several orders of magnitude higher than that of a conventional refractive optic, as

well as a large amount of power passing straight through them. This beam pass-through was the largest with longer-wavelength incident light, as well as with shorter pillar height. The notable exception to these trends was with the wafer with 4.0 μm pillars at 3.39-μm incident light. Measurements for this wafer at this wavelength showed a forward scattering lobe similar in shape to Mie scattering. This particular measurement showed much higher beam pass-through than with the same lens at other wavelengths. All other measurements showed a Lambertian scatter floor underlying their diffraction orders, and followed the beam pass-through patterns mentioned previously.

Future work involving these metasurfaces should include a finer spectral characterization, especially on the wafer with the designed pillar heights, to measure the wavelength range of its forward scattering lobe. The other wafers should also be studied to see if they develop similar lobes at new wavelengths. Additionally, the only scatter measurements taken with these metasurfaces involved a small portion of the lens illuminated by a laser beam, and only the in-plane scatter was collected. Full-width illumination, broad spectrum illumination, and out-of-plane scatter were not characterized in this thesis, and would all make for good follow-up experiments.

Acknowledgements

I would like to acknowledge the tremendously helpful and detailed guidance and feedback provided by my advisor, Dr. Michael Marciniak. Without his help, this thesis would not have been possible. Additional thanks go to Dr. Augustine Urbas for providing the samples measured in this study, as well as one of the lasers.

Matthew R. Miller

Table of Contents

Page

List of Figures

Page

List of Tables

Page

I. Introduction

1.1 Context

Lenses focus light by imparting a parabolic phase curvature to the incoming waves.[1] Traditional spherical lenses have a continuous phase curvature that includes multiples of 2π radians. Fresnel lenses use the same parabolic phase technique but in discrete steps, with each step limited to 2π radians. The sharp edges of a Fresnel lens show the discontinuities of phase, where the optical phase difference returns from 2π back to zero. The phase-delaying elements of a metasurface function in exactly the same way.[2] A phase delay is accumulated along the surface up to 2π radians, and then the pattern is repeated at the designed frequency.

Metasurface lenses are flat surfaces capable of focusing light through phase manipulation, specifically a parabolic phase function.[3] Phase manipulation is achieved through the subwavelength elements that decorate the surface. Each one has a characteristic phase delay that it applies to the incoming wave. Originally, these elements were made of gold.[4] These nano-antennas would absorb incoming light through plasmonic resonance, and re-radiate as a dipole antenna with a designed phase delay. These were deemed too inefficient for practical use: the resonance was dependent on the shape of the antenna and hence the polarization of the incoming light. Therefore, these designs would be 50% efficient at best when working with an unpolarized source. Further, the dipole antenna nature of the elements did not have a directional preference, meaning that the re-radiated light went in all directions, not just forward. Even with perfectly functioning gold elements, the lens could only propagate 25% of the incident power forward.

More recently, the focus has shifted away from plasmonic metasurfaces and more towards dielectric ones[4]. These materials are capable of much higher efficiencies because they are

transparent at their design wavelength. Light passes through them rather than re-radiating from an antenna, meaning that there is a forward directional preference. This alone gives them up to twice the efficiency of plasmonic metasurfaces. This thesis is an attempt to quantify the forward scattering produced by dielectric metasurfaces, as well as the focusing efficiency of metasurface lenses shown by the total integrated scatter.

1.2 Need

Metasurfaces have been fabricated and characterized in many different ways, but their optical scatter has yet to be studied. This is an important area of consideration because excess scatter will increase stray light and noise in an optical system, reducing the signal to noise ratio.

1.3 Task

Three different cylindrical metasurface lenses designed for use in the infrared were characterized using an optical scatterometer. Three different wavelengths of incident light, 3.39, 4, and 5 μm, were used in attempt to characterize a spectral response. The scatter measurements were done using a modified Schmitt Measurement Systems Complete Angle Scan Instrument (CASI). This allows for a complete spatial scan of a sample's scattered light from -90 to 90° on the transmission side of the lens within the plane of incidence. From this, it will be known to what angles light is being scattered and radiated, as well as the power contained within the focal regions.

1.4 Object

Chapter II walks through the background of metasurface development and how these lenses came to be made. As already stated, the first metasurfaces were made of gold nano-

antennas, but the lenses studied in this thesis consist of dielectric elements. Chapter II will provide the history of this transition and why dielectrics have proven themselves to be a more useful alternative to plasmonic elements.

Chapter III will focus specifically on the experimental setup and samples. The three metasurfaces are all dielectric metasurface cylindrical lenses, with elements based on a cylindrical pillar architecture. Varying diameters of cylinders leads to varying phase delays of the elements. The phase front was arranged in such a way as to create a cylindrical lens for characterization. The optical scatter is collected using the CASI and quantified using the bi-directional transmittance distribution function (BTDF).

Chapter IV is the first of the results and analysis chapters. This chapter will compare the scatter observed from metasurfaces with that of a traditional refractive lens. The next section, Chapter V, will be a second study comparing the three metasurfaces against each other. The difference between them all is the depth to which their cylindrical pillar elements are etched. This section will compare their performance when measured away from lens center to blazed diffraction gratings, as well as characterize the amount of beam pass-through each metasurface shows at 3.39, 4, and 5 μm incident laser wavelength.

Chapter VI will include all of the conclusions drawn from the data and analysis. The metasurfaces showed very similar behavior to blazed diffraction gratings when measured away from lens center in the spacing of their respective diffraction orders across all wavelengths tested. This could prove useful if one were to need to separate spectral information while focusing incident light all in one flat optic. However, the power contained within the useful diffraction orders was often unfavorable, and beam pass-through was still an issue. However, two patterns regarding beam pass-through were established: shorter wavelengths and longer

pillar heights lead to decreased beam pass-through, and more of the total integrated scatter is then contained within the first diffraction order, the design order, as one would expect from a blazed diffraction grating. Future work is then discussed at the end of the chapter.

II. Background and Theory

2.1 Chapter Introduction

This chapter will serve as the background to metasurface characterization. First presented will be the history of metasurface development and the generalized law of refraction that they are built upon. Following this, there will be a section on Fresnel lenses to understand the design of the phase delay of metasurface lenses. Next will be a section on blazed diffraction gratings. These metasurface lenses have similar scatter behavior to blazed gratings, and so it is important to understand what they are. Finally, there will be a section describing bi-directional scatter distribution function (BSDF) which will aid in understanding the collected data.

2.2 Metasurfaces

Metasurfaces[1-6] are flat surfaces that use subwavelength scattering elements to manipulate the phase of an incoming wave. Each scattering element has its own characteristic phase delay that it imparts upon its subsection of the incident wave. Therefore, the entire metasurface imparts a discretized phase function upon the entire incident wave. The shape of this phase function is entirely up to the designer of the metasurface[1], and several have already been made, including linear phase shifts for beam steerers, quadratic phase shifts for lenses[1] (see eqs. 1 and 2), and a circularly symmetric linear phase shift for an axicon[7]. However, the primary focus of metasurface design has been with lenses, and this thesis will be no exception.

The idea of metasurfaces first came to light in 2011 with the generalized laws of reflection and refraction by Yu et al.[1] They theorized that Snell's law could be rewritten in terms

of a phase gradient on the boundary between two materials.[1] Their mathematical arguments are summarized below.

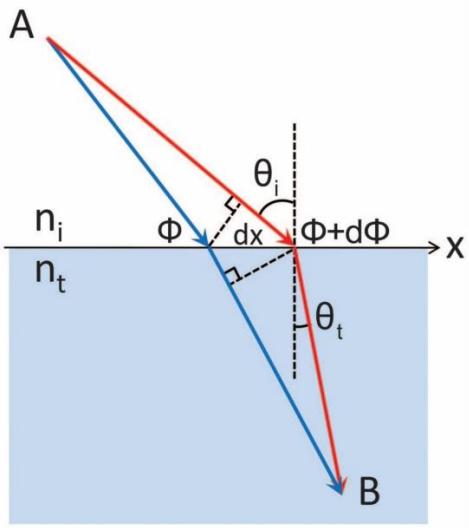

Figure 1. This schematic shows two rays that are infinitesimally separated from each other in both physical space (x) and in phase (ϕ). These rays both cross the material boundary and arrive at the same point because their difference is so infinitesimally small. By using Snell's law of refraction across a boundary, as well as the argument that the two rays are practically identical, equation 1 is derived. From [Yu, N. et. al. Light Propagation with Phase Discontinuities: Generalized Laws of Reflection and Refraction. Science 21 Oct 2011: Vol. 334, Issue 6054, pp. 333-337. DOI: 10.1126/science.1210713]. Reprinted with permission from AAAS.

$$[k_o n_i \sin(\theta_i) dx + (\Phi + d\Phi)] - [k_o n_t \sin(\theta_t) dx + \Phi] = 0 \quad (1)$$

$$\frac{\lambda_o}{2\pi}\frac{d\Phi}{dx} = n_t \sin\theta_t - n_i \sin\theta_i \quad (2)$$

Starting from the equivalent phase argument in equation 1, equation 2 gives the generalized law of refraction for the in-plane direction, which contains Snell's law of refraction in the right side, but now substituting k for $2\pi/\lambda$ tells us is that the direction of refracted light can be controlled through the use of a phase gradient on the boundary between materials.

In the case of a metasurface replicating a spherical lens, the phase profile $\phi(x,y)$ required to focus a normally-incident plane wave of wavelength λ at focal position f is shown by equation 3, where x and y indicate the horizontal and vertical positions on the metasurface, respectively.

Similarly, and more applicable to the metasurfaces studied in this thesis, equation 4 shows the phase profile of a metasurface replicating a cylindrical lens, where x is horizontal position.

$$\phi(x,y) = -\frac{2\pi}{\lambda}\left(\sqrt{x^2+y^2+f^2} - f\right) \tag{3}$$

$$\phi(x) = -\frac{2\pi}{\lambda}\left(\sqrt{x^2+f^2} - f\right) \tag{4}$$

In addition to reflection, Yu et al. further expand these generalized laws to reflection.[1] They explain that, because sine is an odd function and negative angles will give negative values, there will be two different angles of reflection for the same angle of incidence in the opposite direction. For the case of total internal reflection, equation 5 is generated to find the critical angles θ_c.

$$\theta_c = \sin^{-1}\left(\pm\frac{n_t}{n_i} - \frac{\lambda_o}{2\pi n_i}\frac{d\Phi}{dx}\right) \tag{5}$$

Additionally, because of the phase gradient at the boundary, the angle of reflection no longer equals the angle of incidence. The new angle of reflection is given by equation 6.

$$\sin\theta_r - \sin\theta_i = \frac{\lambda_o}{2\pi n_i}\frac{d\Phi}{dx} \tag{6}$$

The final application of the phase gradient boundary was to standard reflection, where the index of refraction is the same on both sides of the boundary, because they are the same material. By applying $n_t=n_i$ to equation 5, Yu et al. explain that "there is always a critical angle of incidence above which the reflected beam becomes evanescent."[1] This critical angle is given by

$$\theta_c = \sin^{-1}\left(1 - \frac{\lambda_o}{2\pi n_i}\left|\frac{d\Phi}{dx}\right|\right) \tag{7}$$

There are two categories of materials used for the scattering elements of a metasurface: plasmonic (metallic) and dielectric. Antennas are one of the more commonly used plasmonic elements due to their simple design and fabrication.[8] The antennas absorb incoming light through charge oscillation, then re-radiate at the same wavelength with a phase delay. The phase delay given by a plasmonic antenna is dependent upon its length, shape, and direction, and these antennas can be linear (similar to a radio antenna) or angled in the middle to form a V, as shown in Figure 2. These V-antenna metasurfaces have been fabricated for a number of different optics, including beam steerers, flat lenses, and flat axicons as previously mentioned. In addition to plasmonic elements, metasurfaces have also been simulated and/or fabricated using a series of apertures through plasmonic material, including slits[9-11], nano-holes[12-14], V-apertures[15], and U-apertures[16]. Plasmonic metasurfaces were designed with a range of applications in mind, but they were not practical due to their poor efficiency.[17,18]

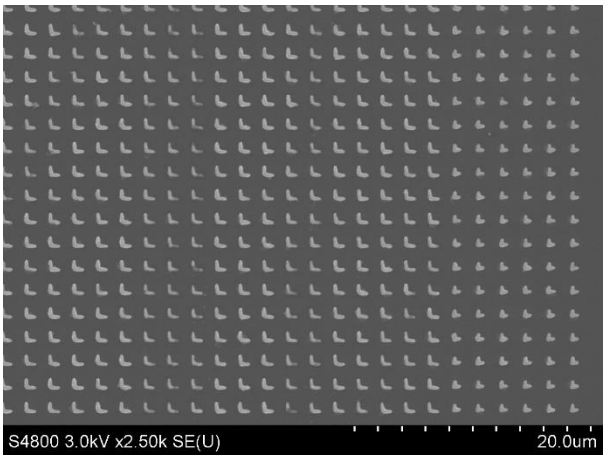

Figure 2. SEM image of gold V-antennas on a metasurface lens.[19]

With efficiency in mind, dielectric elements are now more commonly used.[20] Rather than relying on oscillating charges to generate re-radiation (often, radiation which then propagates in all directions, not just forward), dielectric elements act as microscopic waveguides which passively generate phase delay based on their width and length.[18]

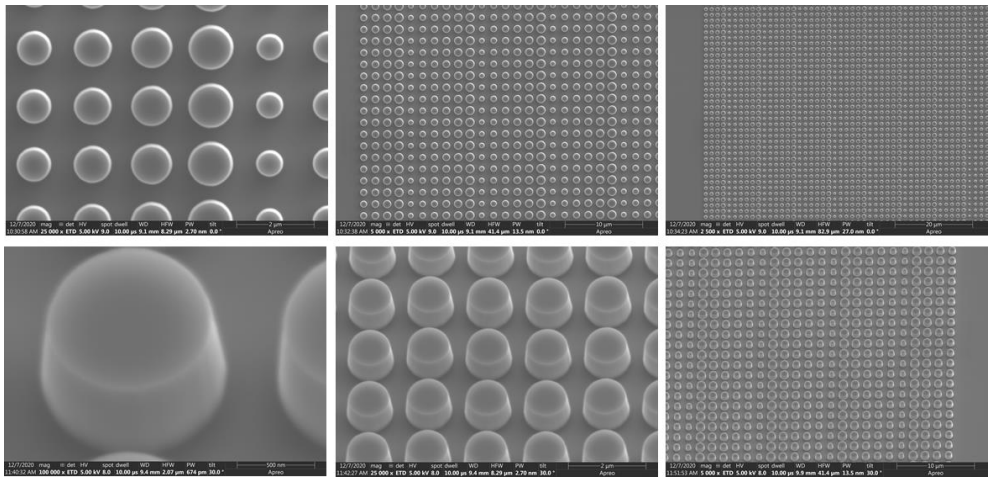

Figure 3. SEM images of dielectric posts arranged on one of the metasurface lenses characterized in this study. These will be explained further in Chapter 3.

A commonly used dielectric element for infrared wavelengths is the cylindrical silicon post[21] (see Fig. 3), which, due to its symmetry, is polarization independent,[22] unlike all of the previous plasmonic element designs. This design is used on the lenses studied in this thesis, and therefore is the most relevant.

2.3 Fresnel Lenses

One thing that all metasurface lens designs have in common is that they all function as Fresnel lenses. The difference between a Fresnel lens and a conventional spherical lens is the magnitude of the phase change created by the lens. A conventional spherical lens continuously

increases the change of phase through several orders of 2π, where a Fresnel lens uses a repeating cycle of phase change from 0 to 2π. Figure 4 visually compares the two types.

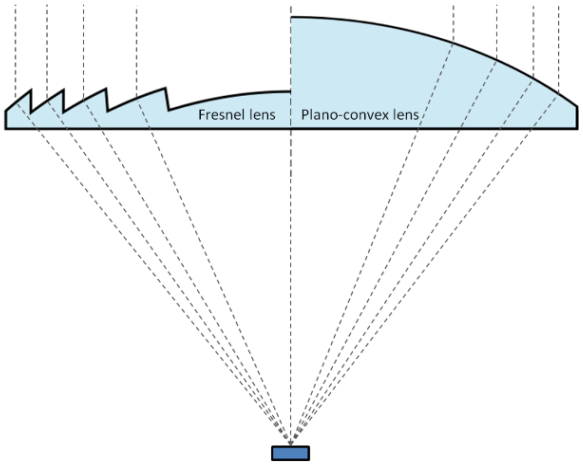

Figure 4. The thickness of the material determines the magnitude of the phase change imparted on an incoming wave. The plano-convex lens smoothly builds up phase delay to a maximum at the center of the lens. The Fresnel lens has a maximum of 2π phase delay at the thickest parts of the lens, and this pattern is repeated to match the overall phase delay of the plano-convex lens.[23]

The biggest advantage to using a Fresnel lens over a spherical lens is the savings in material and weight. A common application of Fresnel lenses is in lighthouses, where the lenses can be several feet across (see Fig. 5). To create a spherical lens of the same diameter, a substantial volume (and therefore mass) of glass would need to be used. Similarly, Fresnel lenses are also used in automobile taillights.

Figure 5. A large-diameter Fresnel lens used in a lighthouse.[24]

In regards to metasurface design, Fresnel lenses are important in the sense that they only use phase delays up to 2π. Metasurface scattering elements are therefore designed to have phase delays up to 2π, then use a repeating set of elements to create the Fresnel lens effect as shown in Fig. 6.

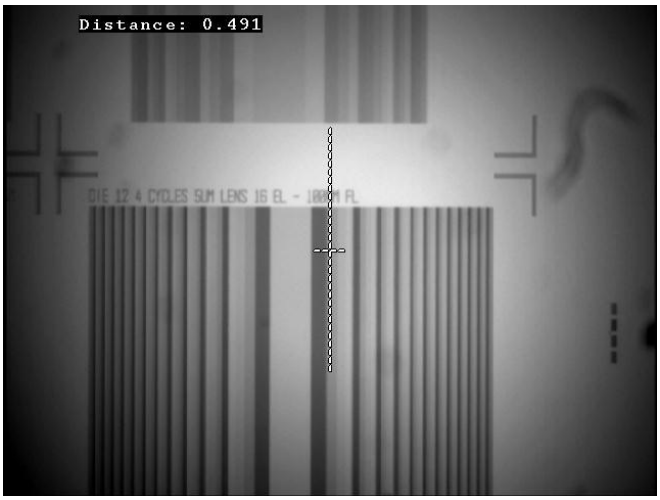

Figure 6. A wider angle view of the plasmonic V-antenna cylindrical Fresnel lens shown in Fig. 2. Here we can see the different zones occupied by different shapes of V-antenna, seen as darker or lighter regions. These regions are wide in the center of the lens, but get narrower when approaching the edges.

The phase zones (also known as Fresnel zones) visible on the SEM image in Figure 6 start out relatively wide at the center of the lens, but decrease in size travelling away from the center. These narrow phase zones each steer the beam in a particular direction, similar in behavior to a blazed diffraction grating.

2.4 Blazed Diffraction Gratings

A repetitive array of diffracting elements, either apertures or obstacles, that has the effect of producing periodic alterations in the phase, amplitude, or both of an emergent wave is said to be a diffraction grating[25]. In practice, common diffraction gratings are transmission gratings and blazed reflection gratings. Transmission gratings use many (often thousands per millimeter) line apertures to create an interference pattern. This pattern consists of several "orders," which are local intensity maxima, and the locations of these orders follows equation 8, known as the grating equation,

$$a \sin\theta_m = m\lambda \tag{8}$$

where the m^{th} diffraction order's angular location θ_m is related to the wavelength λ and the aperture width a. The diffraction orders are counted with integers m=0,±1,±2, … The wavelength dependence of the order location makes diffraction gratings an ideal optic for spectrometers, since the different wavelengths of the light source become physically separated. The problem with transmission gratings is that most of the power is concentrated in the zeroth order where there is no spectral separation.

A blazed diffraction grating is different because it is a reflection grating with angled mirror slits instead of transparent apertures. Blazed gratings follow the same grating equation, but typically have most of their reflected power concentrated in the m=+1 order, rather than the zeroth order like a transmission grating. This positive-side-favoring reflection also reduces the redundant power given to negative orders, therefore higher positive orders receive more power. Higher orders are better for spectroscopy due to their increased spectral separation and therefore higher resolving power.

Relating to metasurfaces, the different phase zones of a Fresnel lens can act like a blazed grating in transmission rather than reflection. The metasurface lenses are transmissive, but the diffraction orders seen in scatter measurements of a non-center portion of the Fresnel lens can favor one side because of the phase gradient within a Fresnel zone, similar to those of blazed gratings.

2.5 Quantifying scatter with BSDF

Bi-directional scatter distribution function (BSDF) compares transmitted radiance L_t to incident irradiance E_i, as shown in equation 9. BSDF is bi-directional because both the incident and the transmitted directions are taken into account in the calculation. The scatter part of the acronym implies that both reflective (BRDF) and transmissive (BTDF) scatter is being considered. For this thesis, only transmitted scatter will be considered, and so bi-directional transmittance distribution function (BTDF) will be used instead.

$$BTDF\ (Sr^{-1}) = \frac{dL_t(W\ cm^{-2}\ Sr^{-1})}{dE_i(W\ cm^{-2})} = \frac{\Phi_t}{\Phi_i cos\theta_t \Omega_d} \tag{9}$$

Transmitted radiance, L_t, is the power transmitted per unit area per solid angle, and incident irradiance, E_i, is incoming power per unit area. These two areas are identical, and so they cancel each other out. Except, the transmitted area is scaled by the viewing angle θ_t, and so the cosine term remains. As shown in Fig. 7, because the detector swings across the entire 180° range of transmission angles and the effective area of the sample spot decreases as viewing angle increases, the $\cos(\theta_t)$ term in equation 9 corrects the power measurements into radiance.

Also shown in Fig. 7, θ_t is the angle between the detector position and the z-axis, the direction of incident light. In practice, BTDF can be written as the right-most equality of equation 9, where transmitted power and incident power are labeled as Φ_t and Φ_i, respectively. The solid angle subtended by the detector is given by Ω_d.

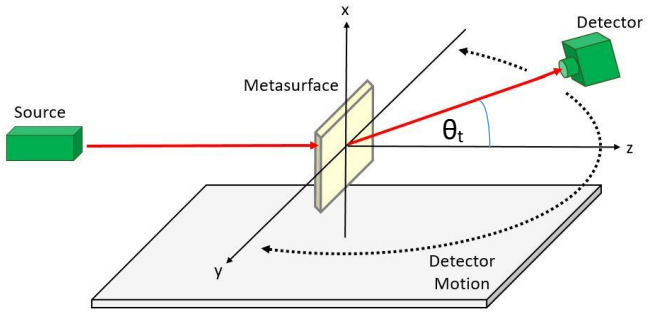

Figure 7. An example of BTDF measurement. In this case, it is the Complete Angle Scatter Instrument (CASI) used in the scatter measurements for this experiment. The CASI will be explained later in Chapter 3.

BTDF is useful for characterizing metasurface lenses because scatter power collected is normalized by the incident power, which means that changing the incident wavelength (thereby changing the laser and its incident power) will not inherently change the BTDF.

2.6 Summary

In this chapter, the history of development of metasurfaces was discussed, followed by a brief overview of Fresnel lenses, blazed diffraction gratings, and BTDF measurements as they apply here to metasurfaces. Understanding these sections is critical to understanding the experimental setup for characterizing the scatter of metasurface lenses and for interpreting the results. In the next chapter, the experimental setup will be explained in greater detail.

III. Methods and Samples

3.1 Chapter Introduction

This chapter continues the discussion of BTDF with the introduction of the CASI, the instrument used to measure BTDF. Further on, the three lasers used to illuminate the metasurfaces will be introduced, followed by the introduction to the metasurfaces themselves.

3.2 CASI

The Complete Angle Scatter Instrument (CASI) is an optical scatterometer (see Figs. 7 and 8) which compares incident light to the light scattered by a sample illuminated by the source. Specifically, the CASI measures bi-directional transmittance distribution function (BTDF) which compares transmitted radiance L_t to incident irradiance E_i, as shown in equation 9. The solid angle subtended by the detector is given by Ω_d in equation 9 and is the area of the detector A_d divided by the squared radius R between the detector and the sample.

$$\Omega_d = \frac{A_d}{R^2} = \frac{\pi D_d^2}{4(0.5m)^2} = \pi D_d^2 \quad (10)$$

In the CASI setup, this radius is fixed at 0.5 m, leading to R^2=0.25, which cancels the 4 in the denominator. The denominator still has units of m^2, and this keeps the overall equation units to m^2/m^2 = Sr. Additionally, the diameter of the aperture is more commonly used throughout the CASI's operating software, and so in equation 10, area of the detector is shown as π*(diameter of the aperture D_d / 2)^2.

The aperture diameters available to the CASI are 0.300, 1.100, 4.075, and 13.850 mm. This corresponds to a Ω_d of $2.83*10^{-7}$, $3.80*10^{-6}$, $5.22*10^{-5}$, and $6.03*10^{-4}$ Sr^{-1}, respectively.

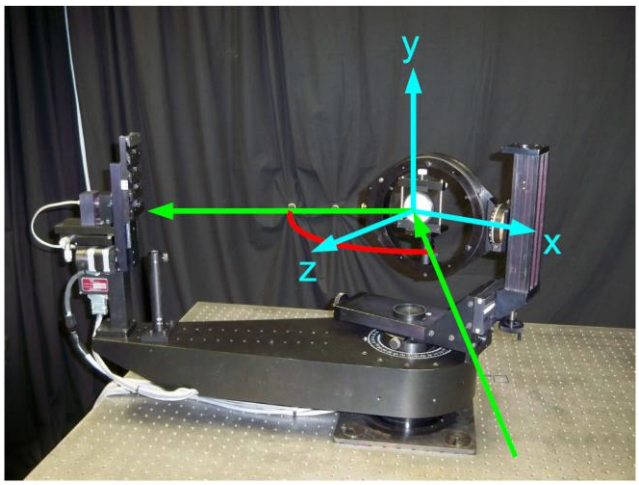

Figure 8. A photograph of the receiving end of the CASI system. Shown here are the rotation and translation stages that hold the sample, as well as the 500 mm rotating arm holding the detector.

The CASI instrument was used to explore the scattering properties of individual subsections of the metasurfaces. The CASI goniometer arm is 500 mm long, far longer than the 40 mm focal length of the metasurface lenses studied. Therefore, it is expected that the beam detected will be focused and then diverged to the CASI detector for lens center measurements or steered away from θ_t=0° for off-center measurements. For example, a beam on the right side of the lens will be steered to the left. The detector will scan from -90 to 90° in transmission (behind the lens) as depicted in Fig. 7.

3.3 Lasers

The CASI system shown in Fig. 8 can be adapted to suit a wide range of wavelengths, all that is needed is the right laser and the right detector. For this study, an Indium Antimonide (InSb) detector was used, along with three wavelengths of mid-wave infrared laser. These were a 3.39 μm Helium Neon laser, a 4 μm ThorLabs diode laser, and a 5 μm Daylight Solutions tunable quantum cascade laser.

3.3.1 Helium Neon Laser

The shortest wavelength used in this study was 3.39 μm, which came from a Research Electro Optics 2.0 mW helium neon (HeNe) gas tube laser, model number 32172. HeNe lasers are more commonly used as visible laser sources with their characteristic 632.8 nm red emission, but the same mixture of gases can be used to produce a 3.39 μm infrared beam instead. This beam incident onto the sample would ideally be collimated in the case of BTDF measurement, however the beam is instead focused to a point at the detector for the purposes of alignment and calibration, which means it is gently converging at the sample.

The degree of convergence can be calculated by using the spot size at the sample position and the 500 mm distance from sample to detector, assuming that the beam focuses to a single point. The spot size of the beam at the sample can be directly measured with a knife edge measurement. This is a fairly simple process where the power at the detector is measured while a knife edge incrementally blocks the beam. In the case of the 3.39 μm beam, the step size (which is also used as the uncertainty of the measurement) of the knife edge was 0.5 mm. The power received (shown on the y-axis of Fig. 9) decreases as the knife edge covers more of the beam.

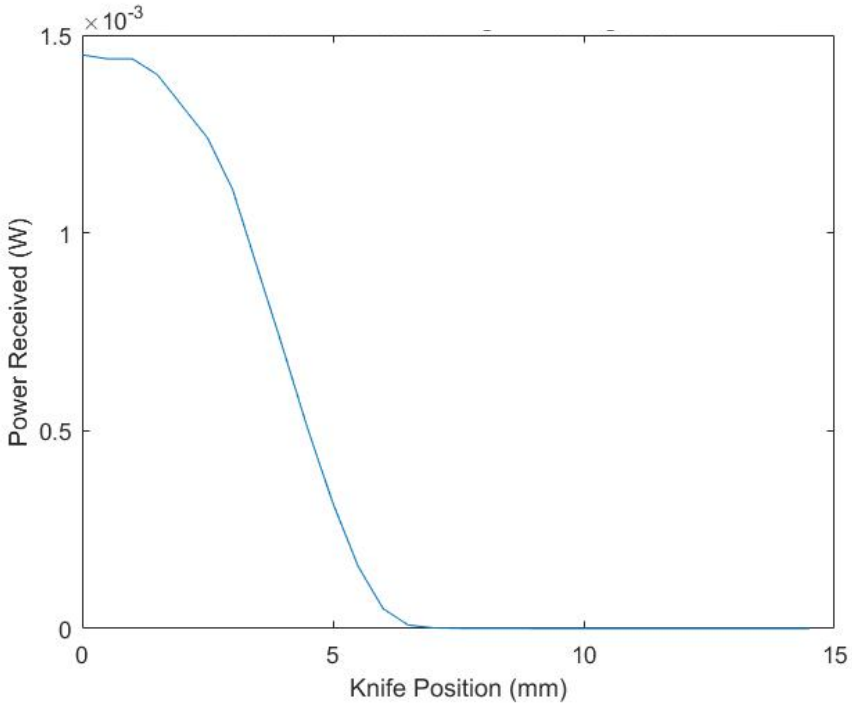

Figure 9. The power received during a knife-edge scan of the 3.39 μm beam. The width of the beam at its $1/e^2$ points is found to be 3.5±0.5 mm.

The full width at half maximum (FWHM) would be the horizontal distance between the points marking 75% and 25% of maximum power received. FWHM will be used later on in this thesis to describe the width of an expanded beam and also diffraction orders. In this case, however, it is more appropriate to use $1/e^2$ points due to the Gaussian shape of the TEM_{00} modes of a laser beam. What this means for knife edge measurements is that instead of 75% and 25% power points, use 88% and 12%. This is a more appropriate measurement of the width of a Gaussian beam because the integrated area within the FWHM of a standard Gaussian curve (at ±0.83σ) is only 76%, whereas using the $1/e^2$ points (±1.41σ) contains 95%.

For the 3.39 μm beam, the width at the $1/e^2$ points is 3.5±0.5 mm at the sample position. The f/# is therefore 500 mm / 3.5 mm = 143. The angle of convergence can be found by doubling

the half angle: $\theta = 2(\tan^{-1}(1.75/500)) = 0.40°$. Finally, the size of the diffraction limited spot at the detector is given by equation 11 as 1182 μm, where f=500mm, λ=3.39μm, and D=3.5mm. This is about four times larger than the smallest aperture available on the CASI system at 300 μm.

$$d = 2.44 \frac{f \lambda}{D} \tag{11}$$

3.3.2 ThorLabs Diode Laser

The middle wavelength of the three used was 4 μm, which was emitted by the QF 4050C2 laser from ThorLabs, which is a small semiconductor laser with a maximum output power of 600 mW. This was also the design wavelength for the metasurfaces.

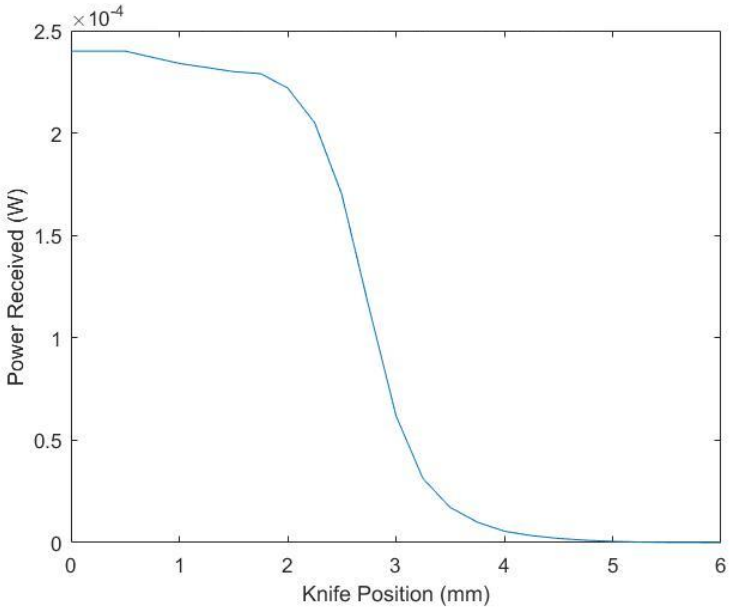

Figure 10. The power received during a knife-edge scan of the 4 μm beam. The width of the beam at its $1/e^2$ points is found to be 1.50±0.25 mm.

At the sample position, the 4 μm beam was measured to be 1.50±0.25 mm at its $1/e^2$ points, as shown by the knife edge scan in Figure 10. This gives the beam a f/# of 333 and a convergence angle of 0.17°. Using equation 11, this time with λ=4μm and D=1.5mm, the diffraction limited spot is d=3253 μm, again much larger than the smallest aperture available to the CASI system.

3.3.3 Daylight Solutions QCL

The longest wavelength used was 5 μm from the Daylight Solutions MIRcat-2100 tunable quantum cascade laser (QCL), with a maximum output power of 400 mW.

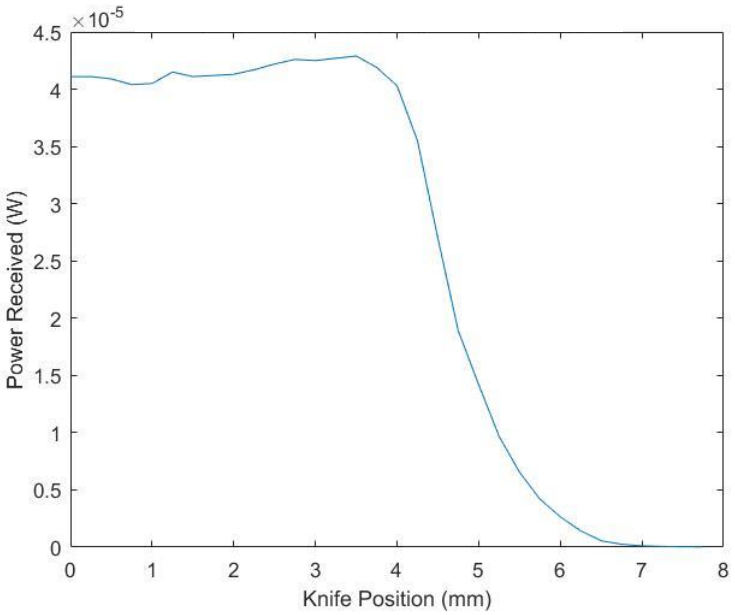

Figure 11. The power received during a knife-edge scan of the 5 μm beam. The width of the beam at its $1/e^2$ points is found to be 1.5±0.25 mm.

At the sample position, the 5 μm beam was measured to be 1.50±0.25 mm at its $1/e^2$ points, as shown by the knife edge scan in Figure 11. This gives the beam an f/# of 333 and a convergence angle of 0.17°. Using equation 11, this time with λ=5μm, the diffraction limited

spot is equal to d=4067 μm, again much larger than the smallest aperture available to the CASI system.

3.4 Samples

The three metasurface lenses studied were all cylindrical lens dielectric metasurfaces based on a nano-pillar Fresnel lens architecture designed by Ekaterina Poutrina and fabricated by Piyush Shah. There are several diameters of pillars (one such pillar shown in Fig. 12 and previously in Fig. 3) being used in each lens ranging from 0.4 to 1.4 μm, with each diameter corresponding to a different phase delay. The phase delays range from 0 to 2π, and re-wrap back to zero in the same way that it would for a conventional Fresnel lens (seen in Fig. 3, Fresnel zones are formed with sections of cylindrical elements that all have the same diameter, and therefore the same phase delay).

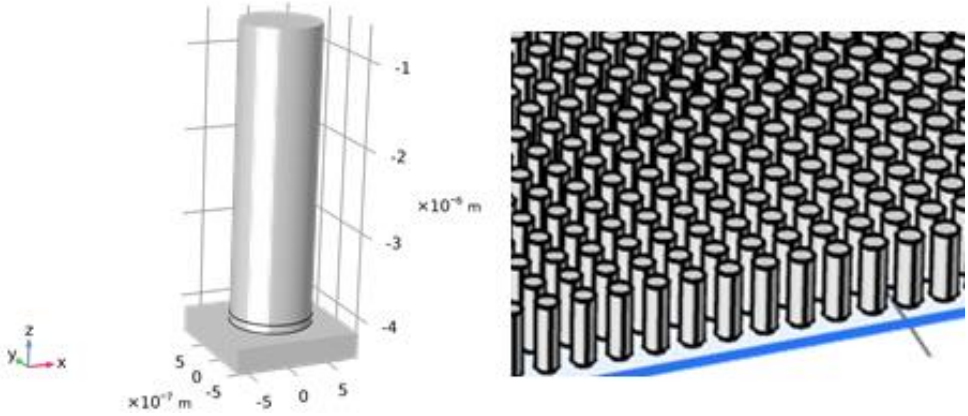

Figure 12. An example of the cylindrical pillar unit cell and a close-up view of the lens surface.

The pillars all have the same height on any particular metasurface. From one metasurface to the next, however, the pillar height changes. The design pillar height was 3 μm, with variations of this design having pillar heights of 1 and 5 μm. The fabricated pillar heights were

found to be 0.9, 4.0, and 5.2 μm, and this discrepancy is likely because there is no etch-stop layer, and so precise etch heights are difficult to achieve. The physical dimensions of the metasurface were 40 mm by 40 mm, with the cylindrical Fresnel lenses designed to have a focal length of 40 mm. Because this is a cylindrical lens, the focused light would form a vertical focal line, rather than a circular focal point.

3.5 Summary

This chapter introduced the methods used to characterize the optical scatter received from three metasurface lenses. Next, the three laser beams and their widths at the sample location were shown, and finally, the samples themselves were introduced. In the next chapter, the results comparing metasurface scatter to conventional refractive lens scatter will be shown.

IV. Data and Analysis: Metasurface Lens Scatter vs. Refractive Lens Scatter

4.1 Chapter Introduction

This chapter begins the presentation of scatter profiles of metasurface lenses in comparison to the blank doubly polished silicon substrate on which they were fabricated and a traditional refractive lens with the same focal length. The measurements shown in this chapter are all taken with the beam incident upon the center of the lenses, and at all three wavelengths.

4.2 Measurements at 4 µm

Figure 13 compares the scatter from the central spots on the three metasurface lenses, the CaF_2 lens, the blank silicon substrate, and the signature scan at 4 µm incident wavelength.

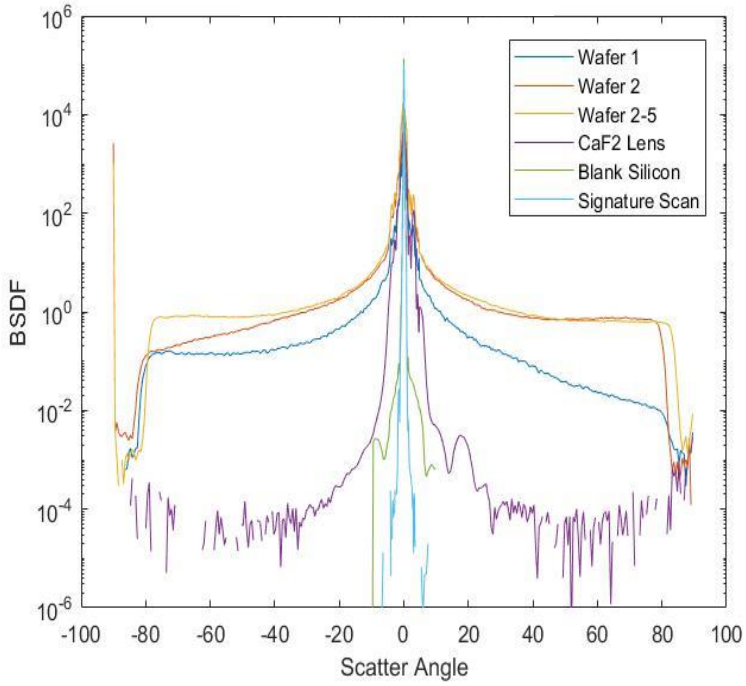

Figure 13. Log-linear plot of wafer 1 (under-etched, 0.9 µm posts), wafer 2 (design, 4.0 µm posts), and wafer 2-5 (over-etched, 5.2 µm posts) compared to their substrate and a calcium fluoride lens of the same focal length. This measurement was done with a 4 µm wavelength laser.

The 4-μm laser spot at the sample was 1.5±0.25 mm using the $1/e^2$ points on a knife-edge scan as discussed in Chapter 3. The innermost blue plot in Fig. 13 is the signature scan, which is a blank scan of the focused beam with no sample in place. As one would expect, the blank scan generally shows the lowest scattering and the narrowest profile. The upper schematic of Fig. 14 shows a diagram of a signature scan. This type of scan uses the full dynamic range of the CASI, about 11 orders of magnitude in BTDF space (see Fig. 13), in the span of about 9°, so a range of $|\theta_t| \leq 4.5°$.

The focused laser beam shows peak BTDF on the order of 10^5 Sr^{-1}, and within this range, drops down to the noise floor on the order of 10^{-6} Sr^{-1}. Taking a signature scan involves first focusing the beam at the detector, then using automated centering tools within the software to align the detector to <0.005° of the true center (smallest step size is 0.003° when using the smallest aperture, 0.3 mm diameter).

While at the center position, total signal is then collected by switching to the largest 13.85 mm aperture and collecting the power. This total signal figure is used in the calculation of BTDF as Φ_i in equation 9. Although the BTDF definition assumes the beam incident on the sample is collimated, it is gently converging in practice to ensure proper calibration of the measurements. The 1.5 mm spot at the sample is focused over a range of 500 mm, the length of the CASI arm, leading to a convergence of f/333.

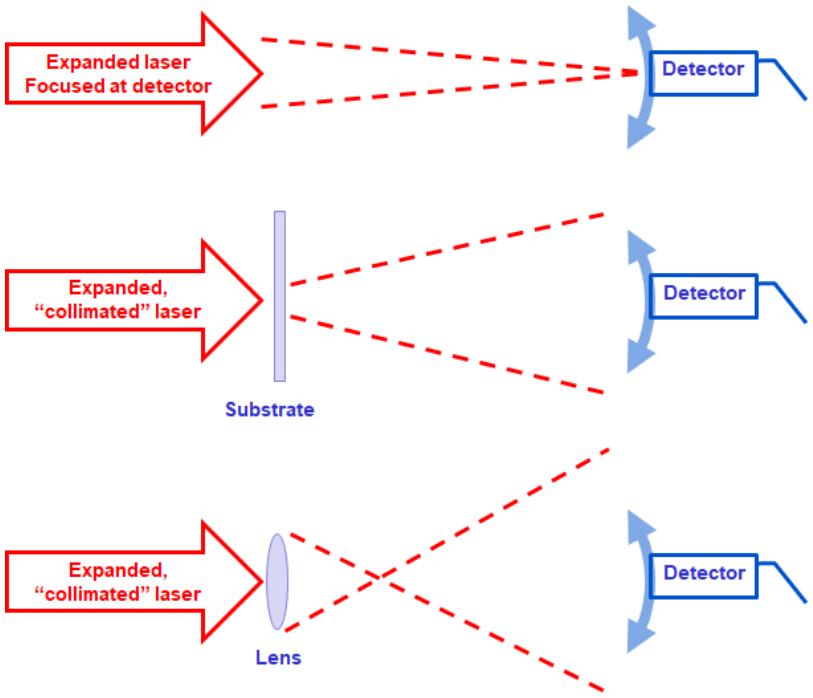

Figure 14. The three different types of scans examined in this study. The top diagram shows a signature scan, where the beam is focused into the detector with a convergence of f/333. The beam is approximated as being collimated at the sample due to this gentle convergence, but is focused as tightly as possible to improve resolution and take advantage of the CASI's high dynamic range. The middle diagram shows transmitted scatter from a flat sample like the blank silicon substrate. The lower diagram shows a geometric representation of our f=4cm lenses being observed from 50 cm away by the detector.

The green plot in Fig. 13 is scatter from the blank silicon substrate on which the metasurfaces were fabricated. The middle diagram in Fig. 14 shows what is being measured in this plot. It is a double-side polished silicon wafer and is extremely transparent in the infrared, as shown by the scan. Extremely specular transmission and reflection measurements are what the CASI is designed to make. This is where the variable step size and high dynamic range are most beneficial. The blank silicon is identical to the signature scan from the scatter peak at 10^{5} Sr^{-1} to six orders of magnitude lower at 10^{-1} Sr^{-1}, where scattering shoulders branch off. Included in these shoulders is only 0.2% of the total integrated scatter (TIS), as defined as the area under the curve outside of the

2° central spot width at BTDF = $3x10^{-2}$ Sr^{-1} normalized by the integrated area under the total curve. In Figure 15, the BTDF near zero degrees for the blank silicon can be seen above that of the signature scan. This is unexpected and likely due to an alignment error.

Continuing outward in Fig. 13 is the violet plot which is scatter from a refractive CaF_2 lens. It shows a wider central scattering pattern due to the focusing and diverging of the incident beam, as shown in the bottom schematic of Fig. 14. The focal length of the lens is 4 cm, and the scatter pattern is being measured at a distance of 50 cm from the lens, so geometric divergence of about 2° is expected. In practice, the measured full-width at half max (FWHM) was 0.98°. The width of the diverged beam can be more clearly seen in Fig. 13 on a log-log scale. The CaF_2 lens is also clean and transparent, and 22% of the TIS is outside of the focused/diverged beam's FWHM. CaF_2 is commonly used in infrared optics, and is expected to have a consistent behavior across a wide range of infrared wavelengths. For this reason, this lens was only measured at 4 μm incident wavelength.

4.3 Metasurface Scatter at 4 μm from centers of lenses

All three of the metasurfaces show much higher scattering at wide angles ($|\theta_t| > 30°$ in Figs. 13 and 15) than the blank silicon substrate or the CaF_2 lens. These are the flat shoulders at BTDF $\cong 10^{-1} – 10^{0}$ Sr^{-1} in Fig. 13. Flat curves on BTDF plots like this indicate Lambertian-like, rather than forward scatter. Wafer 1, the under-etched sample with 0.9 μm-tall posts as opposed to the 3 μm-tall design, shows scattering about three orders of magnitude higher than the CaF_2 lens (about 10^{-1} Sr^{-1} versus 10^{-4} Sr^{-1}), and wafers 2 and 2-5 (with 4.0 and 5.2 μm posts, respectively) show very similar performance to each other, both having scatter about four orders of magnitude greater than the CaF_2 lens (about 10^{0} Sr^{-1} versus 10^{-4} Sr^{-1}).

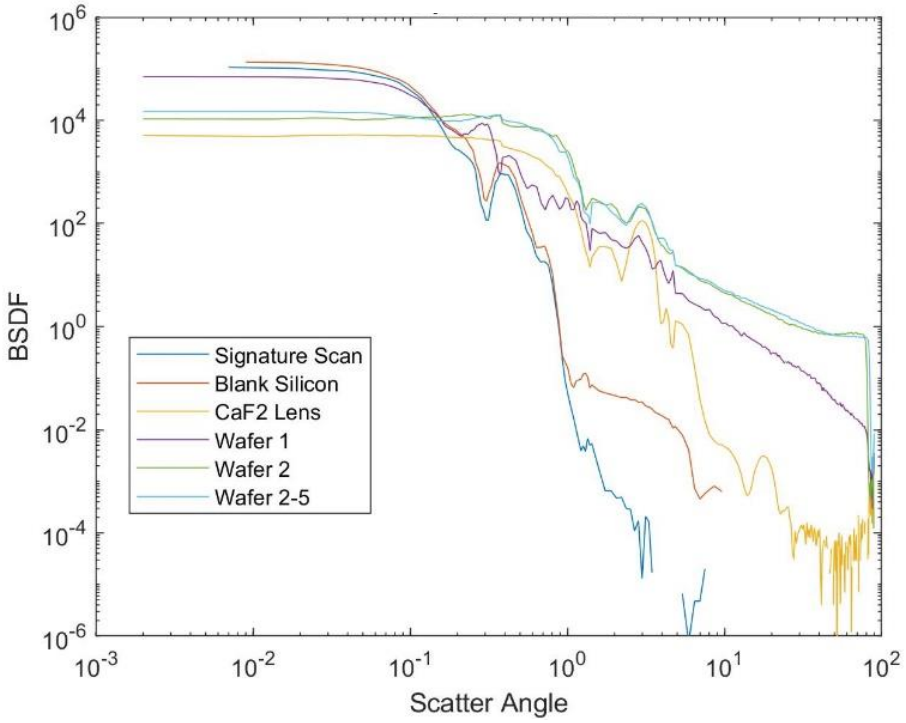

Figure 15. Log-log plot showing the positive angle side of Figure 13. This figure more clearly illustrates the behavior of the scatter near θ_t=0° at 4 μm wavelength, including the scattering shoulders of blank silicon breaking away from the signature scan at 10^{-1} Sr^{-1}.

The scattering near θ_t=0° is easiest to read on the log-log plot of Fig. 15. The over-etched and design lenses (wafers 2 and 2-5) show nearly identical scattering, with focused/diverged beams of FWHM=1.2°, following a similar pattern to the CaF_2 (FWHM=0.9°), but with the individual scattering elements (the nanopillars discussed in Chapter 3) raising the shoulders up by four orders of magnitude in BTDF space, from about 10^{-4} Sr^{-1} for CaF_2 to about 10^{0} Sr^{-1}. That being said, only 28% of the TIS for these two metasurfaces was outside of their FWHM, an increase of only 6% over that of the CaF_2 lens.

The under-etched lens (wafer 1) is where performance deteriorates, shown not only by the increased scatter floor of the metasurface, but also by its central beam in Fig. 15 with FWHM=0.2°,

similar to that of the signature scan and silicon substrate. This implies that the under-etched metasurface is scattering the light, but not efficiently focusing it. As a result, although the scatter floor of wafer 1 at about 10^{-1} Sr^{-1} in BTDF space is below those of wafers 2 and 2-5 (~10^{0} Sr^{-1}) in Fig. 13, 39% of the TIS from wafer 1 (under-etched) was outside of its FWHM.

4.4 Measurements at 3.39 µm

The 3.39 µm laser spot at the sample was 3.5±0.25 mm using the $1/e^2$ points on a knife-edge scan as described in Chapter 3. The innermost blue plot in Fig. 16 is the signature scan, which again is a blank scan of the focused beam with no sample in place. The focused laser beam shows peak BTDF on the order of 10^{6} Sr^{-1}, then drops down to the noise floor of approximately 10^{-5} Sr^{-1} in this case. Again, although the BTDF definition assumes the beam incident on the sample is collimated, it is gently converging in practice, about f/286 in this case due to the wider beam at the sample location.

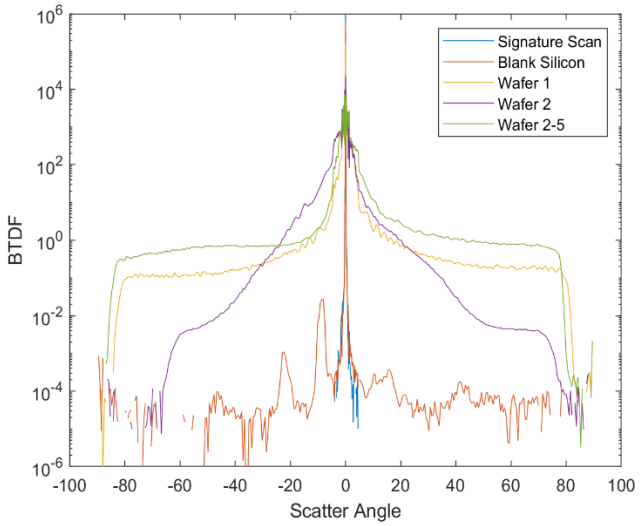

Figure 16. Log-linear plot of wafer 1 (under-etched, 0.9 µm posts), wafer 2 (design, 4.0 µm posts), and wafer 2-5 (over-etched, 5.2 µm posts) compared to their substrate and a calcium fluoride lens of the same focal length. This measurement was done with a 3.39 µm wavelength laser.

The red plot in Fig. 16 is scatter from the blank silicon substrate on which the metasurfaces were fabricated. Again, it is a double-side polished silicon wafer and is extremely transparent in the infrared, as shown by the scan. The blank silicon is very similar to the signature scan (see Fig. 15) from the scatter peak at 10^5 Sr^{-1} to nine orders of magnitude lower at 10^{-4} Sr^{-1}, where scattering shoulders branch off. Included in these shoulders is only 0.7% of the total integrated scatter (TIS), as defined as the area under the curve outside of the 2.5° central spot width at BTDF = $1x10^{-4}$ Sr^{-1} normalized by the integrated area under the total curve.

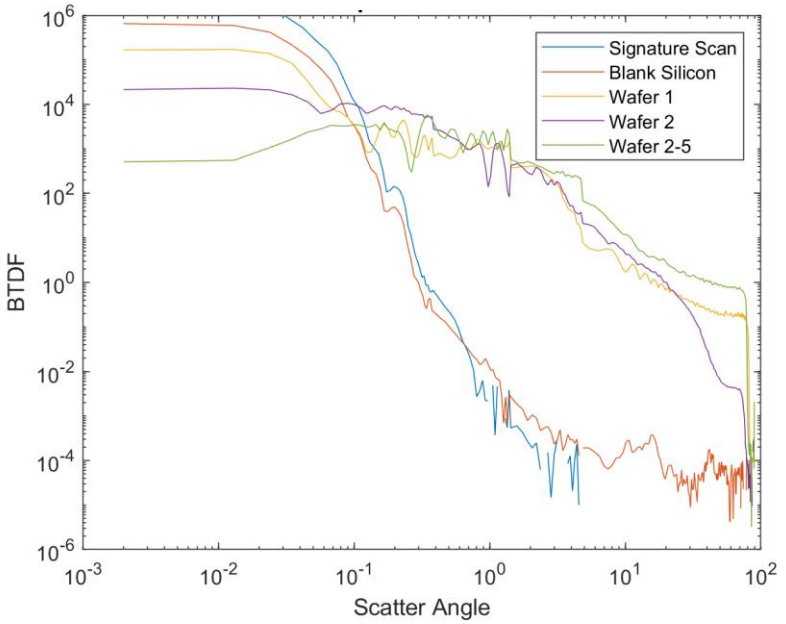

Figure 17. Log-log plot showing the positive angle side of Figure 16, which shows wafer 1 at 3.39 μm.

4.5 Metasurface Scatter at 3.39 μm from centers of lenses

The metasurface scatter at 3.39 μm incident wavelength is unique for wafer 2, the metasurface with 4.0 μm etch depth. This scatter pattern shows a forward scattering lobe which is not seen in either of the other two metasurfaces, or at any other wavelength tested. Because of this,

it is expected that this scatter pattern is a resonant feature, and may be possible to recreate with the other metasurfaces at different wavelengths. This resonant feature is also seen later in Chapter 5 when observing off-center scatter.

As for wafers 1 and 2-5, the scatter patterns have not changed substantially from those seen at 4 μm incident wavelength, with Lambertian outer shoulders and a central peak.

4.6 Measurements at 5 μm

The 5 μm laser spot at the sample was 1.5±0.25 mm using the $1/e^2$ points on a knife-edge scan. The innermost blue plot in Fig. 18 is the signature scan, which is a blank scan of the focused beam with no sample in place. As one would expect, the blank scan shows the lowest scattering and the narrowest profile. The focused laser beam shows peak BTDF on the order of 10^6 Sr^{-1}, and within this range, drops down to the noise floor on the order of 10^{-5} Sr^{-1}.

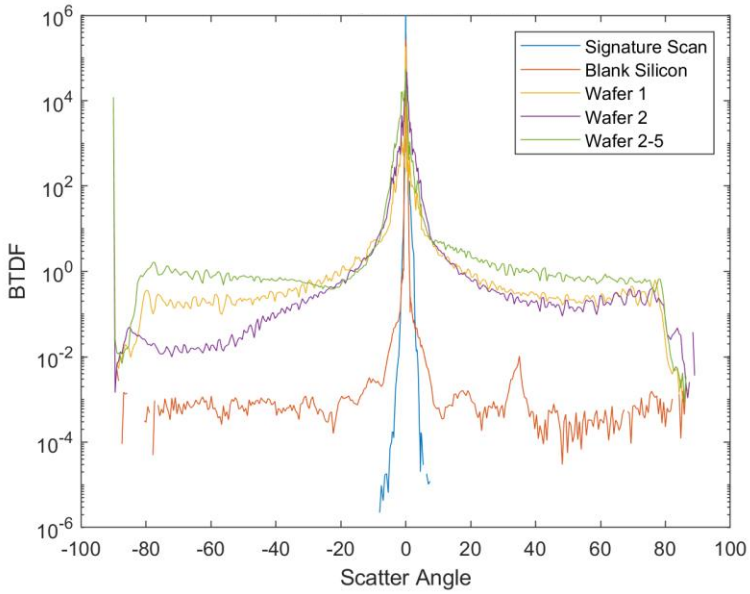

Figure 18. Log-linear plot of wafer 1 (under-etched, 0.9 μm posts), wafer 2 (design, 4.0 μm posts), and wafer 2-5 (over-etched, 5.2 μm posts) compared to their substrate and a calcium fluoride lens of the same focal length. This measurement was done with a 5 μm wavelength laser.

The red plot in Fig. 18 is scatter from the blank silicon substrate, which is similar to the signature scan from the scatter peak at 10^{5} Sr^{-1} to six orders of magnitude lower at 10^{-1} Sr^{-1}, where scattering shoulders branch off. Included in these shoulders is only 0.01% of the total integrated scatter (TIS), as defined as the area under the curve outside of the 2.3° central spot width at BTDF = $1x10^{-1}$ Sr^{-1} normalized by the integrated area under the total curve.

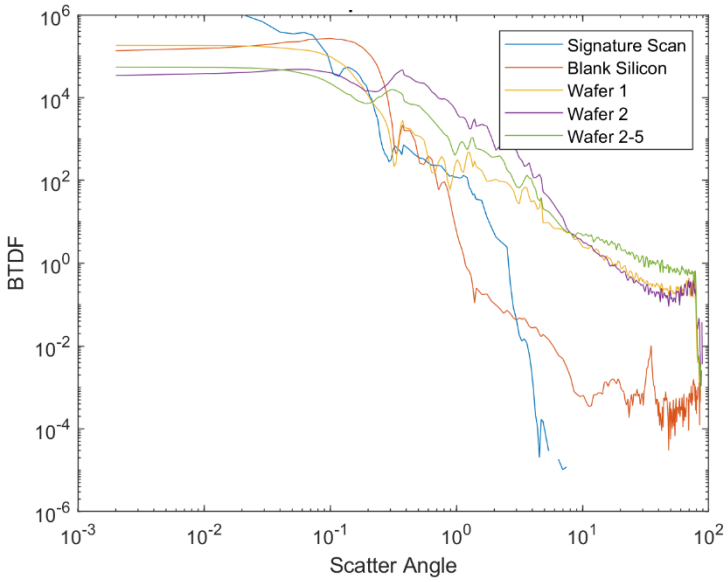

Figure 19. Log-log plot showing the positive angle side of the 5 µm measurements shown in Figure 18.

4.7 Metasurface Scatter at 5 µm, from centers of lenses

All three of the metasurfaces show much higher scattering at wide angles ($|\theta_t| > 30°$) than the blank silicon substrate or the CaF_2 lens. These are the flat shoulders at BTDF ≅ 10^{-1} – 10^{0} Sr^{-1} in Fig. 19. Flat curves on BTDF plots like this indicate Lambertian-like, rather than forward, scatter. Wafer 1, the under-etched sample with 0.9 µm-tall posts as opposed to the 3 µm-tall design, shows scattering about three orders of magnitude higher than that of the CaF_2 lens (10^{-1} Sr^{-1} vs 10^{-}

^{4} Sr^{-1}), and wafers 2 and 2-5 (with 4.0 and 5.2 μm posts, respectively) show very similar performance to each other, both having scatter four orders of magnitude greater than the CaF_2 lens (10^{0} Sr^{-1} vs 10^{-4} Sr^{-1}).

The scattering near θ_t=0° is easiest to read on the log-log plot, as shown in Fig. 19. All three metasurfaces showed significant beam pass-through, showing FWHM<0.2°, in contrast to the CaF_2 (FWHM=0.9°). This implies that the under-etched metasurface is scattering the light, but not efficiently focusing it.

4.8 Chapter Conclusion

As expected, the wide-angle scatter shown by metasurfaces is higher than that of conventional optics. Each of the metasurface lenses showed wide angle scatter at least three orders of magnitude higher than that of the calcium fluoride lens. Additionally, the FWHM of the scatter pattern shows the focusing performance of each lens. When the FWHM is less than that of the CaF_2 lens (0.9°), the incident light continues focusing to a point at the detector, rather than focusing and diverging as one would expect light from a lens to do. When the FWHM is similar to or greater than 0.9°, this is indicative that the lens is focusing as intended. What this means is that all three metasurfaces showed very poor focusing at 3.39 and 5 μm, and the under-etched lens showed poor focusing at 4 μm as well. From the central beam position, only the design-etch and over-etched lenses performed well, and even then, only at the design wavelength of 4 μm.

V. Data and Analysis – Etch Depths among Metasurfaces

5.1 Chapter Introduction

This chapter will showcase the scatter patterns for each of the three metasurfaces at 3.39, 4, and 5 μm incident wavelength with beams incident upon the centers of the metasurface Fresnel lenses and at +1 and +2 cm from the centers. Several diffraction orders from the various Fresnel zones are observed in each measurement, and so naturally, these diffraction orders will be compared with their expected positions given the grating equation and the known spacing of the phase zones in the lens design. This spacing is not a constant quantity, because the spacing decreases in width away from the center of the lens. This creates a slightly chirped blazed grating, and therefore the phase zone spacing is not constant throughout the width of the incident beam. A wider beam creates a larger standard deviation in the average zone size, and this is shown in Table 1.

Table 1. The average phase zone size for each beam and beam location is shown next to its respective standard deviation. A wider beam illuminates a wider range of phase zones which leads to this higher standard deviation.

	3.5 mm beam (3.39 μm wavelength) average zone spacing	Standard deviation in zone spacing	1.5 mm beam (4 and 5 μm wavelength) average zone spacing	Standard deviation in zone spcaing
+1 cm	16.5 μm	1.60 μm	16.5 μm	0.69 μm
+2 cm	9.28 μm	0.20 μm	9.08 μm	0.08 μm

In the last section of this chapter, the amount of beam pass-through will be compared with each lens and wavelength to establish a pattern to help minimize beam pass-through for future metasurfaces.

5.2 Scatter Measurements at 4 μm wavelength

The first wavelength to be discussed will be the design wavelength for the metasurfaces of 4 μm. The previous section showed scatter profiles of the lenses with a centered incident beam. Fig. 21 shows how scatter changes when the 1.5 mm width 4 μm wavelength beam interrogated sections of wafer 2 (4.0 μm post height) located at 1 and 2 cm from the center along this 4 cm wide lens. By translating horizontally along the lens, it is expected that the focused/diverged beam will also shift in the opposite direction (see Fig. 20). The center spot of the lens was found by carefully adjusting horizontal position until maximum transmissive power was found using the CASI software. Maximum power lines up well with central position because the beam is not being steered in either direction when at the center of the lens, and is allowed to transmit directly to the detector, which is where the beam was originally aligned. The outer edges of the beam will be steered in opposing directions and therefore away from the detector, but maximum power will be achieved when the peak intensity of the beam is aligned with the central horizontal position of the lens. This central position is accurate to within approximately ±0.5 mm due to the fluctuating nature of live power measurements.

Horizontal translations away from center are accurate to within ±0.05 mm, as these separation distances were measured using a micrometer. Vertical translation is not being considered, as the metasurfaces were designed as cylindrical lenses, therefore vertical translation illuminates identical elements and serves to study the repeatability of the fabrication.

Figure 20. Different spot positions along the lens are expected to steer the beam as well as focus/diverge the spot size. As shown, the beam positions are at 0, ±1, and ±2 cm. The beam stays in line with its original alignment, but the lens is translated horizontally.

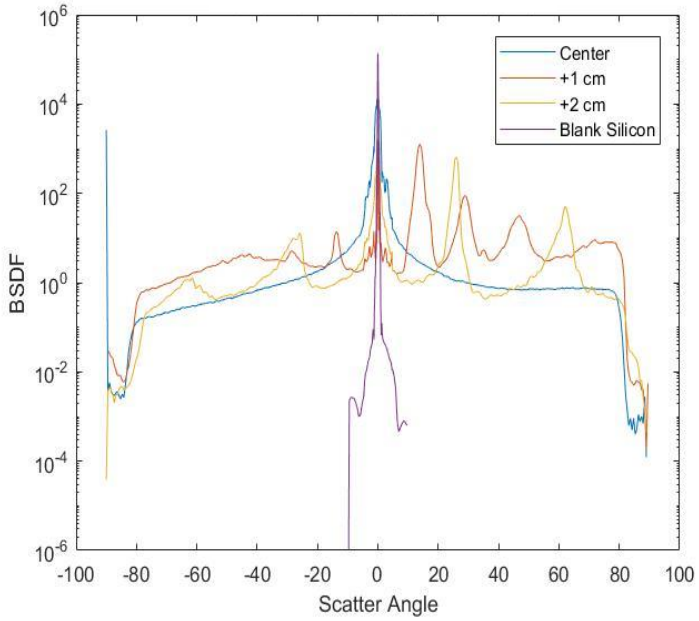

Figure 21. Semi-log plot showing wafer 2 (design post height) scatter at 4 μm with the incident beam at three different locations. These are compared with the scattering seen with blank silicon.

Figure 21 shows measurements of wafer 2, with pillar heights of 4.0 μm, closest to the design 3-μm pillar height, at the design wavelength of 4 μm. Rather than a single focal spot, diffraction orders are measured for these metasurfaces. The diffraction orders on the positive angle side of the scan contain more energy, and in this way the Fresnel lens appears to be a gently chirped, blazed diffraction grating (see Fig. 22). There are still diffraction orders in the negative angle space,

though these contain far less energy, which is also a characteristic of blazed gratings. Also shown in Fig. 21 is the comparison to the blank silicon substrate at 4 μm.

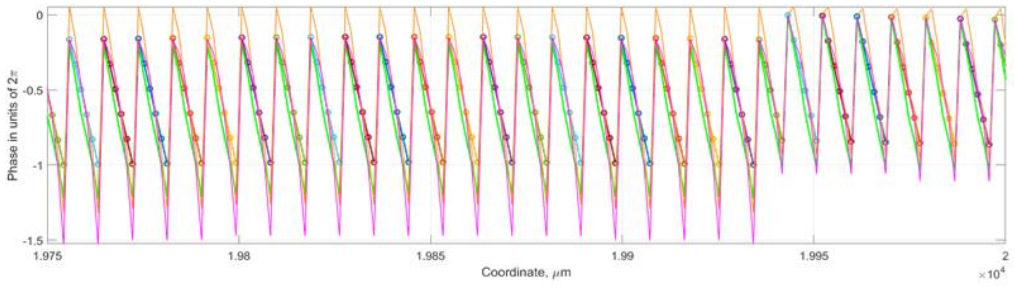

Figure 22. Each point in this sawtooth chart gives the phase delay and horizontal position of an individual scattering element on the metasurface. Every tooth is the beginning of a new Fresnel zone. This image shows how closely spaced the Fresnel zones are at the edge of the lens at +20,000 μm = +2 cm.

The Fresnel zones of the metasurface are larger in the center of the lens, and get smaller going outward. In Fig. 21, at +1 cm horizontal position on the lens, a 1.5 mm spot covers approximately 90 Fresnel zones, giving an average zone spacing of 16.5±1.6 μm (see Table X). At +2 cm, half of the 1.5 mm spot (with the center position of the beam at +2±0.05 cm, half of the beam is on the metasurface and half is illuminating blank silicon) covers approximately 83 Fresnel zones, with an average zone spacing of 9.08±0.08 μm. Using equation 8 and the calculated average Fresnel zone spacings, the positions of the expected diffraction orders are compared in Table 1 to their measured positions.

The relative energy measured for each diffraction order, again defined as the integrated area under a peak between the FWHM, normalized by the integrated area under the total curve, is also shown in Table 1, and compared to the theoretical relative energy in each diffraction order of an ideal blazed grating. The experimental and theoretical diffraction order locations line up very well with each other, however the power contained within each order is far from ideal. A significant

(typically 50% or more) portion of the total integrated scatter is contained within the zeroth order. For a traditional blazed grating, there should be very little power in the zeroth and negative orders, and the majority of the power should be in the $+1^{st}$ order (see Table 1 for details). Although too much power is in the zeroth order, the blaze does appear to be working. Ignoring the zeroth order, the most power of any of the diffraction orders goes into the +1 order, and very little is contained in the negative orders. The notable exceptions to this is the over-etched lens at +1 cm position, which shows 1.13% TIS in the zeroth order and 66.3% in the first order, and also the design-etch lens at +1 cm position, showing 5.67% and 59.1% TIS in zeroth and first orders, respectively. These numbers are still far off from the theoretical TIS expected in the respective zeroth and first orders, but far closer than any other measurements at 4 μm wavelength. Overall, the orders line up in position with traditional diffraction gratings, but the power contained in them is not symmetric about the zeroth order as in a transmissive grating, so the metasurfaces simulate blazed gratings instead.

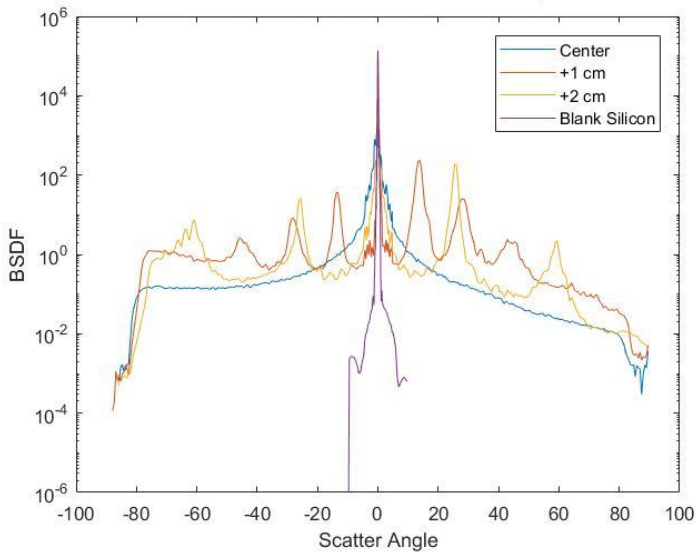

Figure 23. Semi-log plot showing wafer 1 (shorter-than-design post height) scatter at 4 μm with the incident beam at three different locations. These are compared with the scattering seen with blank silicon.

The under-etched lens wafer 1 shows increased power in the negative diffraction orders over the design etch wafer 2. The scatter contained within these orders is quantified in table 2, and visually displayed in Figure 23. Even with the shorter pillar heights, the metasurface still shows diffraction orders located according to the grating equation. The difference between this lens and the design etch in performance is that the under-etched metasurface shows greater beam pass through into the zeroth order, and more scatter into the negative orders. This implies that the grating behavior is still present, but the blazed grating behavior is not. Furthermore, as seen in Chapter 4, the lensing performance is compromised by the increased beam pass through.

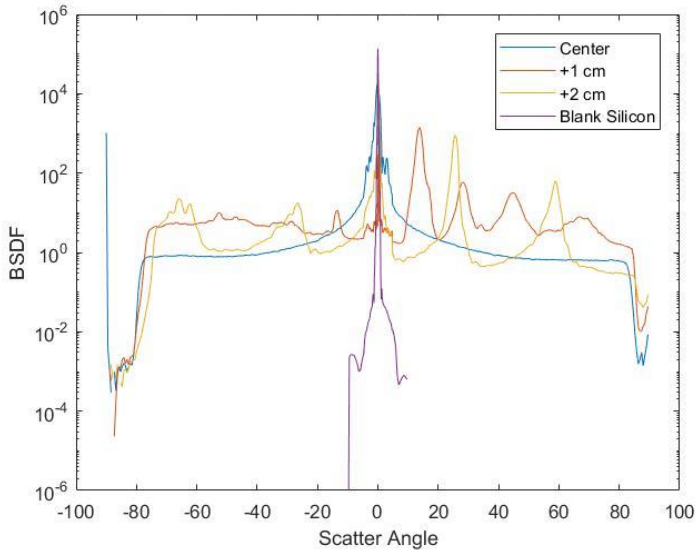

Figure 24. Semi-log plot showing wafer 2-5 (taller-than-design post height) scatter with the 4μm incident beam at three different locations. These are compared with the scattering seen with blank silicon.

In contrast, Figure 24 shows the same measurement but now with the over-etched metasurface lens. In this measurement, the majority of the TIS is contained within the FWHM of the first diffraction order, rather than the zeroth order. The beam pass through is very limited (quantified in Table 1) and the negative diffraction orders are barely visible even on a logarithmic scale. This

implies that the longer post heights of the over-etched metasurface produce better lensing, and a scatter pattern more reminiscent of a blazed grating, rather than a transmissive grating pattern shown in the under-etched metasurface.

5.3 Scatter Measurements at 3.39 μm wavelength

Table 3 shows the same type of measurement data as Table 2, but this time the incident wavelength is 3.39 μm. In general, the results of these measurements are similar to those at 4 μm with most of the TIS being contained within the zeroth order, again with the exception of the over-etched metasurface. The over-etched lens shows the majority of power is contained in the first diffraction order, and strangely, no negative diffraction orders. It is possible that the negative orders are present, but too low power to be detected, which would make the over-etched lens at 3.39 μm wavelength the closest representation of a blazed grating out of all the measurements.

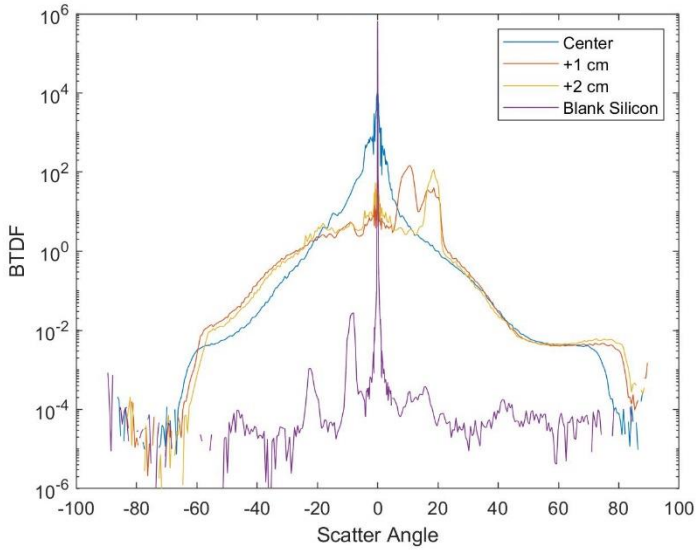

Figure 25. Semi-log plot showing wafer 2 (design post height) scatter with the incident beam at 3.39 μm at three different locations. These are compared with the scattering seen with blank silicon.

The first of the 3.39 μm measurements is wafer 2, the design etch depth. These scatter measurements are unique in the way that a forward scattering lobe is also observed at higher scatter angles. No other metasurface and no other wavelength presents this same pattern. Other measurements show a flat plateau of Lambertian scattering with diffraction orders built on top. Wafer 2 at 3.39 μm however, shows a rounded hump of forward scattering with diffraction orders built on top. The lensing performance was poor, and worse at this wavelength than at 4 μm. Quantified in Table 3, the zeroth order scatter has increased, and the first order scatter has decreased.

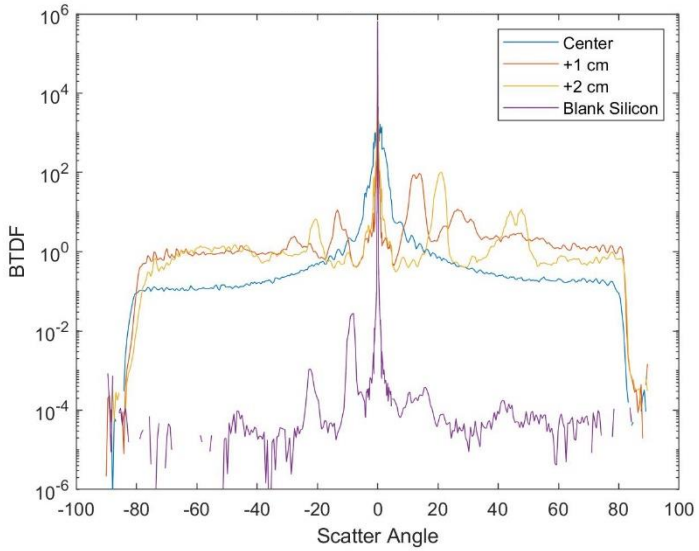

Figure 26. Semi-log plot showing wafer 1 (shorter-than-design post height) scatter with the incident beam at 3.39 μm at three different locations compared to blank silicon.

The under-etched metasurface returns to the standard flat plateau of Lambertian scattering with diffraction orders stacked on top as seen in Fig. 26. This implies that the forward scattering lobe is not a characteristic of the wavelength or the laser (or the wider 3.5 mm beam present with this laser) itself, but rather a combination of the wavelength the post height of the metasurface,

likely a resonant combination. The under-etched lens also shows larger negative orders than the design etch lens, implying although the diffraction orders are strongly present, the grating blaze is ineffective. The scatter contained within these orders is again quantified in Table 3.

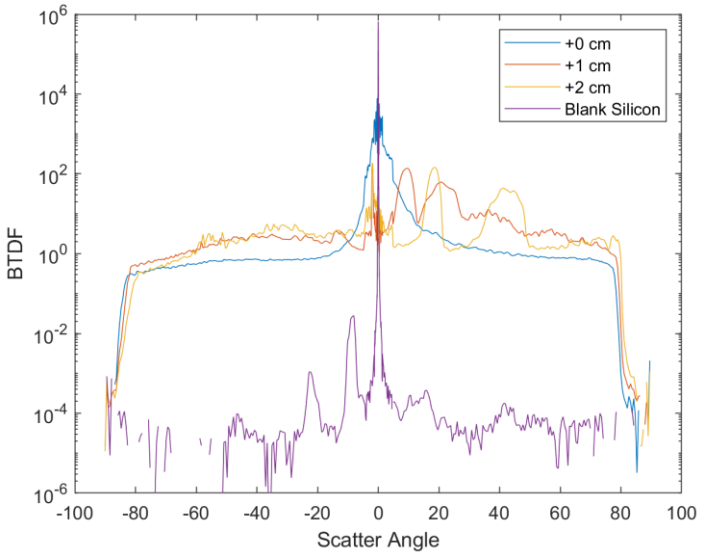

Figure 27. Semi-log plot showing wafer 2-5 (taller-than-design post height) scatter with the incident beam at 3.39 μm at three different locations. These are compared with the scattering seen with blank silicon.

The over-etched metasurface repeats its best-in-class performance at 3.39 μm. Shown in Fig. 27, any negative diffraction orders that are present are not visibly noticeable even on a logarithmic scale. The scatter contained within the FWHM of the positive diffraction orders has decreased from 4 μm wavelength, but there is still substantially more scatter contained in the first positive diffraction order compared to the zeroth order (comparing Tables 2 and 3). In this way, the over-etched metasurface performs the best out of the three metaurfaces tested, and is the Fresnel lens which most closely resembles a blazed grating.

5.4 Scatter Measurements at 5 μm wavelength

Table 4 is the same as Tables 2 and 3, but now changing wavelength again to 5 μm. At this wavelength, the metasurfaces still show blazed grating behavior in the sense that the positive diffraction orders contain more power than the negative diffraction orders, but at 5 μm, the zeroth order contains more power than any of them. The design-etch and over-etched designs, which previously had shown the most power in the first order, now have zeroth orders larger than their first orders. The under-etched lens, which under-performed in the first two wavelengths, continues to do so. Overall, 5 μm wavelength shows the greatest beam pass-through and therefore the worst lensing performance.

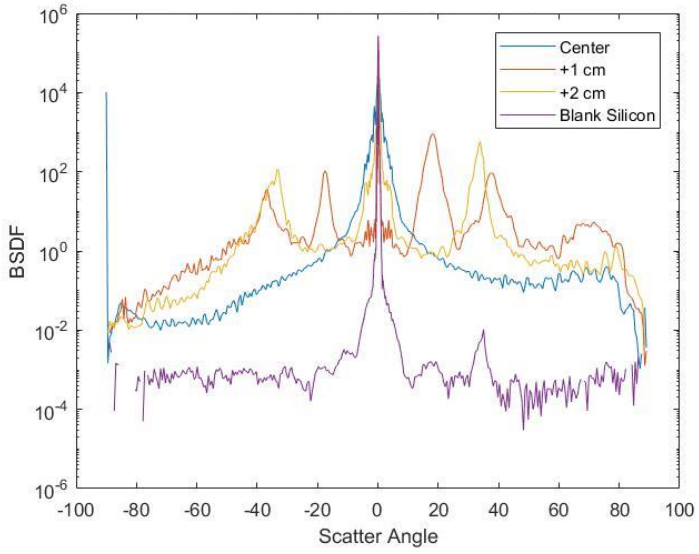

Figure 28. Semi-log plot showing wafer 2 (design post height) scatter with the incident beam at 5 μm at three different locations. These are compared with the scattering seen with blank silicon.

Figure 28 shows the scatter patterns of the 5 μm beam incident upon the design-etch metasurface, wafer 2. This wavelength shows the largest negative diffraction orders, and as shown

in Table 4, the most scatter contained within the zeroth order as well. All of these factors combine to say that 5 μm is the worst performing wavelength out of the three tested for this metasurface.

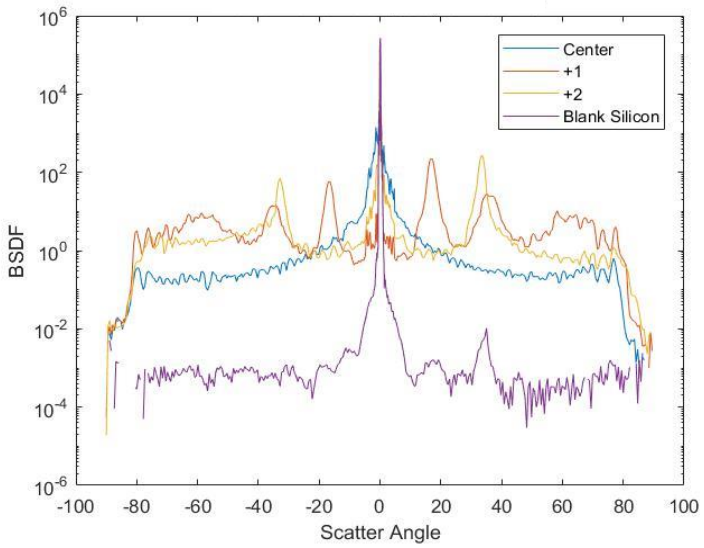

Figure 29. Semi-log plot showing wafer 1 (shorter-than-design post height) scatter with the 5-μm incident beam at three different locations. These are compared with the scattering seen with blank silicon.

In Figure 29, nearly equal-height positive and negative diffraction orders are seen for the under-etched metasurface at 5 μm incident wavelength. The positive orders still contain more scatter as shown in Table 4, so the lens still performs as a blazed grating, albeit very poorly and only if the zeroth order is removed. The under-etched metasurface at 5 μm is the worst combination of lens and wavelength in terms of beam pass-through, with over 79% of the scatter being contained within the FWHM of the zeroth order for both the +1 cm and +2 cm beam locations.

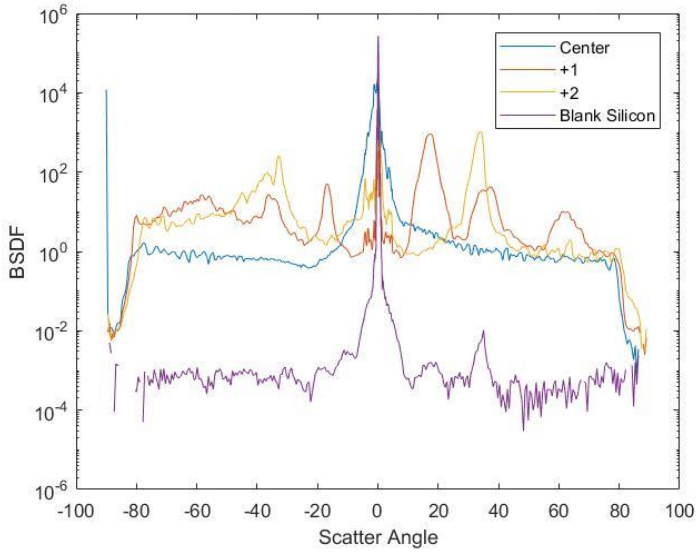

Figure 30. Semi-log plot showing wafer 2-5 (longer-than-design post height) scatter with the incident beam at 5 μm at three different locations. These are compared with the scattering seen with blank silicon.

Figure 30 shows the scatter patterns for the over-etched metasurface at 5 μm incident wavelength. In previous plots of this lens, the negative diffraction orders were practically indistinguishable from the Lambertian scatter shoulders. At this longer wavelength, negative orders are clearly visible, though they still contain little power compared to their respective positive orders (see Table 4 for details). Following the pattern of the other metasurfaces at this wavelength, 5 μm shows the highest recorded beam pass-through out of the three wavelengths tested, with 43% TIS within the FWHM of the zero-angle peak for the +1 cm measurement, and 51% TIS for the +2 cm measurement. This is also the only measurement that shows the over-etched metasurface containing more scatter within the zeroth order than the first positive order for both beam locations (comparing the bottom two rows of Tables 2, 3, and 4). These factors, along with those from the other two metasurfaces, make it clear that 5 μm is the worst performing of all wavelengths tested.

5.5 Straight-through Power

Straight-through power and beam pass-through have been used interchangeably throughout this thesis, and this section will focus in on the data for this subject. The TIS contained within the zero-angle peak of the +1 cm beam location measurements will be compared across lenses and wavelengths to establish a pattern of beam pass-through, and how this problem can be reduced. It has been stated previously in Chapter 2 that beam pass-through is a recurring problem with metasurfaces, and any solutions discovered here may prove valuable to the greater metasurface community.

Tables 5, 6, and 7 all contain the FWHM for each lens' diffraction orders at a particular wavelength. Recall that without a sample in place, the beam presented by the CASI is focused at the detector. Narrower zeroth order widths imply that the zeroth order is not a proper diffraction order, and instead a measurement of the focused beam passing through the lens. The positive and negative observed diffraction orders have been included in Tables 5, 6, and 7 for because the width of the zeroth order should be on the same order as they are.

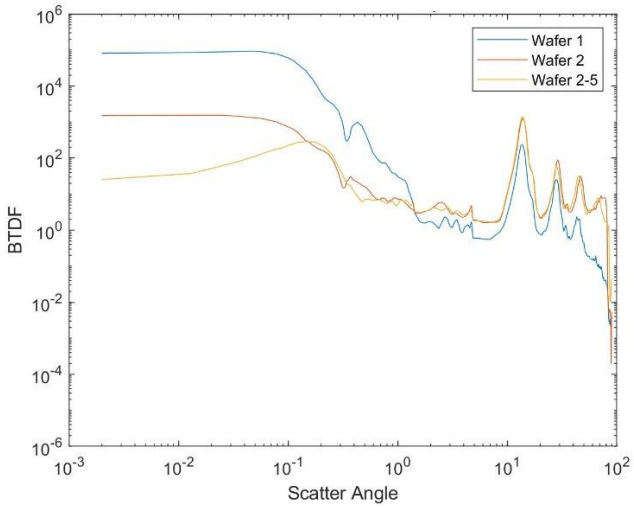

Figure 31. Log-log plot of all three wafers at 4 μm wavelength with the beam placed at +1 cm along the lens.

Figure 31 compares the three metasurfaces with the 4 μm beam at the +1 cm location on a log-log plot. The purpose of doing this is to more clearly show the scatter contained within the zeroth order and visually show the change in beam pass-through from one etch depth to the next. As a reminder, wafer 1 is the under-etched metasurface, wafer 2 is design etch, and wafer 2-5 is the over-etched metasurface lens. The scatter profiles of the three lenses are similar to each other at angles >1°, but closer to zero they separate into three distinct layers which line up in order of etch depth. The under-etched lens wafer 1 shows the highest beam pass-through, and the over-etched lens shows the least, but the over-etched has a null at the center indicating that diffraction is playing a part in this peak. The TIS contained within the FWHM of each measurement's pass-through can be seen in Table 8. Note that the peaks of the first diffraction orders for wafers 2 and 2-5 have a larger magnitude BTDF than their respective zero-angle peaks, and this is reflected in their relatively low beam pass-through in Table 8.

Table 8. The percentage of total integrated scatter contained within the FWHM of the central peak at 4 μm wavelength and +1 cm beam position is shown with respect to each lens.

Wafer	**%BTDF in central lobe**
1	76%
2	6%
2-5	1%

Next, at 5 μm, the three lenses are compared in Figure 32. With the increased beam pass-through of the 5 μm beam, the zeroth order peaks have the larger magnitude BTDF than the first order peaks, in contrast to the 4 μm measurements. This is shown directly in Table 9, where the

percentage of BTDF contained in the FWHM of the zero-angle peak is higher than with either of the other two wavelengths tested.

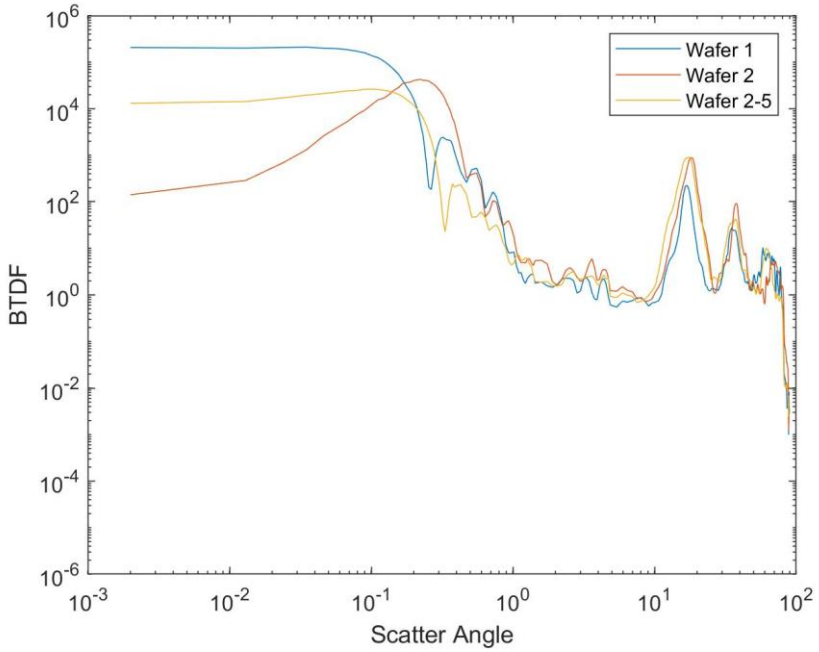

Figure 32. All wafers shown with a 5 μm incident beam at +1 cm position.

Table 9. The TIS contained within the central peaks from each lens when illuminated with a 5 μm beam at +1 cm horizontal position.

Wafer	%BTDF in central lobe
1	79%
2	54%
2-5	43%

Finally, at 3.39 μm wavelength, the beam pass-through levels are at their lowest, with the exception of wafer 2. Wafer 2 is an exception in this case because of the forward scattering lobe present, which gives increased scatter levels at angles closer to zero. This is expected to be a resonant feature of this type of metasurface, because a forward scattering lobe is not seen at any other etch depth or wavelength. Nevertheless, wafers 1 and 2-5 both show their lowest beam pass-

through levels out of the three wavelengths tested. Seen in Figure 33, the zeroth order for wafer 2-5 is so low that it is in-line with the wide-angle scatter shoulders. Because of this, the zeroth order contains very little scatter, at only 0.03% of the TIS (see Table 10).

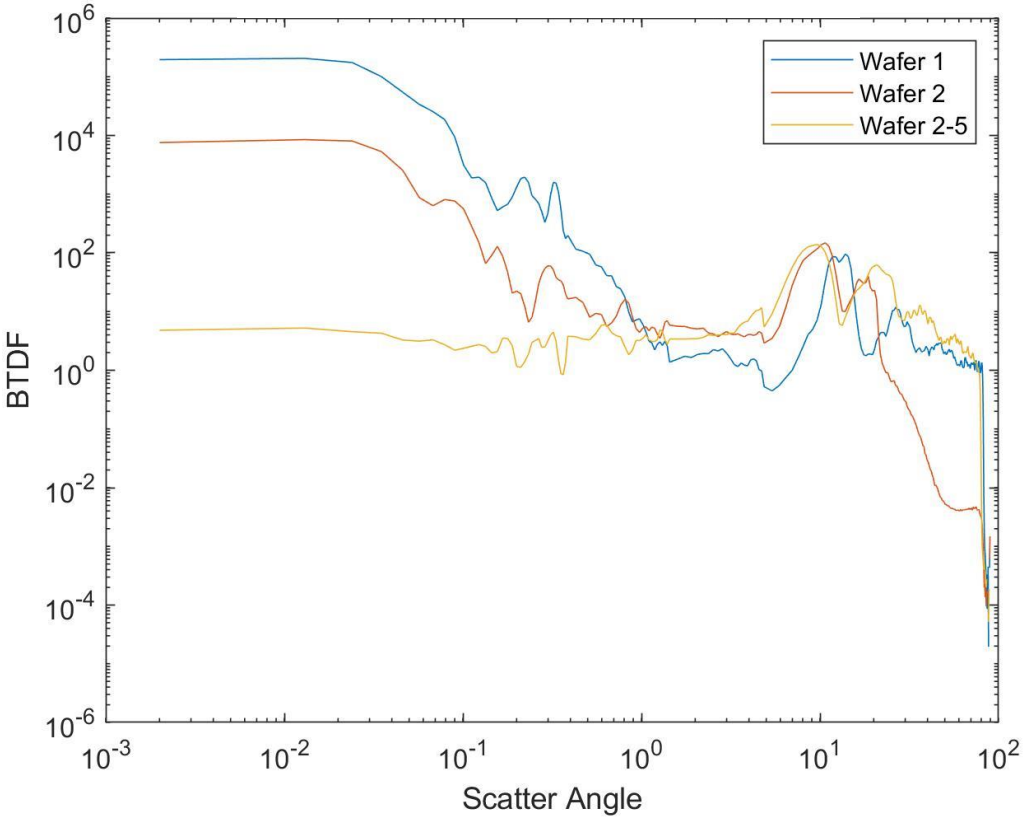

Figure 33. All wafers with 3.39 µm incident beam at +1 cm horizontal position.

Table 10. Each of the three metasurfaces is shown next to its respective percentage of beam pass-through

Wafer	**%BTDF in central lobe**
1	72%
2	32%
2-5	0.03%

As the last three figures and tables have shown, a pattern is emerging with regards to etch depth, wavelength, and beam pass-through. With the one exception of wafer 2 at 3.39 µm, two

patterns can be seen: shorter wavelength and deeper etch-depth lead to decreased pass-through. There are at most only three data points supporting either of these patterns, therefore these are not rock solid conclusions. More detailed characterization should be done to formally nail down these conclusions, and this would likely be finer spectral characterization using tunable lasers rather than attempting to finely adjust the etch depth during fabrication.

5.6 Chapter Conclusion

An incident wavelength of 4 μm (the design wavelength) in general gives the best performance with these metasurface lenses. The beam pass-through is lower than with 5 μm, and the forward scattering lobe seen with 3.39 μm is not seen at this wavelength. Of course, if the design pillar height were more closely met (3.0 μm instead of 4.0 μm with wafer 2) this could all change. The shorter wavelength at 3.39 μm gave the lowest beam pass-through (with the exception of wafer 2), and overall very predictable blazed grating behavior from wafer 2-5, the over-etched metasurface. Increasing the wavelength to 5 μm gave substantially increased straight-through scatter, and so it is not recommended that longer-than-design wavelengths be used for these metasurfaces.

Table 2. Locations of diffraction orders found at 4 μm compared with the expected results from Equation 3, as well as the theoretical and experimental power contained within the FWHM of each order.

Etch = 4 μm, λ=4 μm	**-2nd Order**		**-1st Order**		**0th Order**		**1st Order**		**2nd Order**		**3rd Order**	
+1 cm	N/A	N/A	-14°	7.2e-3	0.01°	5.7e-2	13.9°	5.9e-1	28.9°	6.4e-2	46°	3.7e-2
Theory	-29°	9.4e-4	-14°	8.6e-5	0°	9.6e-5	14°	9.7e-1	29°	5.0e-3	47°	1.4e-2
+2 cm	-63°	7.9e-4	-27°	3.9e-3	0.07°	5.4e-1	26.0°	8.7e-2	62.0°	9.0e-3	N/A	N/A
Theory	-55°	7.2e-3	-24°	8.1e-4	0°	8.3e-4	24°	9.5e-1	55°	3.9e-2	N/A	N/A
Etch = 0.9 μm	**-2nd Order**		**-1st Order**		**0th Order**		**1st Order**		**2nd Order**		**3rd Order**	
+1 cm	-28°	1.3e-3	-14°	4.1e-3	0.04°	7.6e-1	13.6°	2.7e-2	27.9°	5.0e-3	44°	7e-4
+2 cm	-62°	1.3e-3	-26°	2.5e-3	0.08°	6.4e-1	25.8°	1.7e-2	59.1°	3e-4	N/A	N/A
Etch = 5.2 μm	**-2nd Order**		**-1st Order**		**0th Order**		**1st Order**		**2nd Order**		**3rd Order**	
+1 cm	N/A	N/A	-14°	6.3e-3	0.15°	1.1e-2	14.4°	6.6e-1	28.1°	4.2e-2	45°	3.3e-2
+2 cm	-66°	6.3e-3	-27°	6.3e-3	0.18°	4.7e-1	25.5°	1.5e-1	58.8°	1.2e-2	N/A	N/A

Table 3. Locations of diffraction orders found at 3.39 μm compared with the expected results from Equation 3, as well as the theoretical and experimental power contained within the FWHM of each order.

Etch = 4 μm, λ=3.39 μm	**-2nd Order**		**-1st Order**		**0th Order**		**1st Order**		**2nd Order**		**3rd Order**	
+1 cm	-20°	1.0e-2	-10°	2.1e-2	0.01°	3.2e-1	10.2°	3.5e-1	17.8°	1.2e-1	N/A	N/A
Theory	-24°	9.4e-4	-12°	9.6e-5	0°	9.6e-5	12°	9.7e-1	24°	5.0e-3	47°	1.4e-2
+2 cm	N/A	N/A	-19°	1.5e-2	0.02°	4.8e-1	18.6°	2.0e-1	N/A	N/A	N/A	N/A
Theory	-48°	7.2e-3	-22°	8.1e-4	0°	8.3e-4	22°	9.5e-1	48°	3.9e-2	N/A	N/A
Etch = 0.9 μm	**-2nd Order**		**-1st Order**		**0th Order**		**1st Order**		**2nd Order**		**3rd Order**	
+1 cm	N/A	N/A	-13°	1.7e-3	0.01°	7.2e-1	13.6°	2.5e-2	26.6°	4.0e-3	N/A	N/A
+2 cm	N/A	N/A	-21°	8.0e-4	0.02°	6.9e-1	20.7°	1.1e-2	45.9°	2.0e-3	N/A	N/A
Etch = 5.2 μm	**-2nd Order**		**-1st Order**		**0th Order**		**1st Order**		**2nd Order**		**3rd Order**	
+1 cm	N/A	N/A	N/A	N/A	0.03°	3.0e-4	9.1°	3.2e-1	21.8°	2.6e-1	N/A	N/A
+2 cm	N/A	N/A	N/A	N/A	-2.0°	6.8e-2	18.4°	3.5e-1	42.4°	2.3e-1	N/A	N/A

Table 4. Locations of diffraction orders found at 5 μm compared with the expected results from Equation 3, as well as the theoretical and experimental power contained within the FWHM of each order.

Etch = 4 μm, λ=5 μm	**-2nd Order**		**-1st Order**		**0th Order**		**1st Order**		**2nd Order**		**3rd Order**	
+1 cm	-37°	6.8e-3	-18°	1.6e-2	0.2°	5.4e-1	18°	1.9e-1	37°	2.4e-2	N/A	N/A
Theory	-37°	9.4e-4	-17°	9.6e-5	0°	9.6e-5	17°	9.7e-1	37°	5.0e-3	65°	1.4e-2
+2 cm	N/A	N/A	-33	5.1e-3	0.3°	3.6e-1	34°	2.4e-2	N/A	N/A	N/A	N/A
Theory	N/A	N/A	-33°	8.1e-4	0°	8.3e-4	33°	9.5e-1	N/A	N/A	N/A	N/A
Etch = 0.9 μm	**-2nd Order**		**-1st Order**		**0th Order**		**1st Order**		**2nd Order**		**3rd Order**	
+1 cm	-35°	1.4e-3	-17°	2.9e-3	0.02°	7.9e-1	17°	1.1e-2	35.8°	3.0e-3	N/A	N/A
+2 cm	N/A	N/A	-33°	3.5e-3	0.03°	8.0e-1	33°	1.4e-2	N/A	N/A	N/A	N/A
Etch = 5.2 μm	**-2nd Order**		**-1st Order**		**0th Order**		**1st Order**		**2nd Order**		**3rd Order**	
+1 cm	-35°	1.1e-2	-17°	1.1e-2	0.1°	4.3e-1	17.3°	2.9e-1	36.1°	2.3e-2	62.0°	6.0e-3
+2 cm	N/A	N/A	-33°	3.0e-2	0.1°	5.1e-1	33.7°	1.6e-1	N/A	N/A	N/A	N/A

Table 5. Locations of diffraction orders found at 4 μm as well as the FWHM of each order.

Etch = 4 μm, λ=4 μm	**-2nd Order**		**-1st Order**		**0th Order**		**1st Order**		**2nd Order**		**3rd Order**	
+1 cm	N/A	N/A	-14°	2.6°	0.01°	0.18°	13.9°	2.1°	28.9°	3.7°	46.4°	5.8°
+2 cm	-63°	10.6°	-27°	4.8°	0.07°	0.18°	26.0°	2.1°	62.0°	3.1°	N/A	N/A
Etch = 0.9 μm	**-2nd Order**		**-1st Order**		**0th Order**		**1st Order**		**2nd Order**		**3rd Order**	
+1 cm	-28°	3.1°	-14°	2.6°	0.04°	0.17°	13.6°	2.6°	27.9°	3.7°	43.5°	6.3°
+2 cm	-62°	4.8°	-26°	2.5°	0.08°	0.17°	25.8°	2.1°	59.1°	2.6°	N/A	N/A
Etch = 5.2 μm	**-2nd Order**		**-1st Order**		**0th Order**		**1st Order**		**2nd Order**		**3rd Order**	
+1 cm	N/A	N/A	-14°	2.6°	0.15°	0.19°	14.4°	3.2°	28.1°	3.2°	44.8°	4.8°
+2 cm	-66°	3.2°	-27°	4.8°	0.18°	0.25°	25.5°	2.1°	58.8°	2.1°	N/A	N/A

Table 6. Locations of diffraction orders found at 3.39 μm as well as the FWHM of each order.

Etch = 4 μm, λ=3.39 μm	**-2nd Order**		**-1st Order**		**0th Order**		**1st Order**		**2nd Order**		**3rd Order**	
+1 cm	-20°	6.3°	-10°	7.4°	0.01°	0.07°	10.2°	4.2°	17.8°	5.8°	N/A	N/A
+2 cm	N/A	N/A	-19°	4.8°	0.02°	0.06°	18.6°	3.2°	N/A	N/A	N/A	N/A
Etch = 0.9 μm	**-2nd Order**		**-1st Order**		**0th Order**		**1st Order**		**2nd Order**		**3rd Order**	
+1 cm	N/A	N/A	-13°	3.2°	0.01°	0.06°	13.6°	5.8°	26.6°	5.3°	N/A	N/A
+2 cm	N/A	N/A	-21°	3.7°	0.02°	0.06°	20.7°	3.2°	45.9°	6.9°	N/A	N/A
Etch = 5.2 μm	**-2nd Order**		**-1st Order**		**0th Order**		**1st Order**		**2nd Order**		**3rd Order**	
+1 cm	N/A	N/A	N/A	N/A	0.03°	0.05°	9.1°	4.2°	21.8°	8.5°	N/A	N/A
+2 cm	N/A	N/A	N/A	N/A	-2.0°	0.62°	18.4°	3.7°	42.4°	8.5°	N/A	N/A

Table 7. Locations of diffraction orders found at 5 μm as well as the FWHM of each order.

Etch = 4 μm, λ=5 μm	**-2nd Order**		**-1st Order**		**0th Order**		**1st Order**		**2nd Order**		**3rd Order**	
+1 cm	-37°	3.2°	-18°	2.1°	0.2°	0.19°	18°	3.2°	37°	3.7°	N/A	N/A
+2 cm	N/A	N/A	-33	2.1°	0.3°	0.14°	34°	2.1°	N/A	N/A	N/A	N/A
Etch = 0.9 μm	**-2nd Order**		**-1st Order**		**0th Order**		**1st Order**		**2nd Order**		**3rd Order**	
+1 cm	-35°	4.8°	-17°	2.6°	0.02°	0.20°	17°	2.6°	35.8°	5.8°	N/A	N/A
+2 cm	N/A	N/A	-33°	2.1°	0.03°	0.25°	33°	2.1°	N/A	N/A	N/A	N/A
Etch = 5.2 μm	**-2nd Order**		**-1st Order**		**0th Order**		**1st Order**		**2nd Order**		**3rd Order**	
+1 cm	-35°	5.3°	-17°	2.6°	0.1°	0.20°	17.3°	3.7°	36.1°	6.3°	62.0°	7.4°
+2 cm	N/A	N/A	-33°	1.5°	0.1°	0.19°	33.7°	2.6°	N/A	N/A	N/A	N/A

VI. Conclusion

Three different dielectric metasurface lenses designed for use in the infrared were characterized at three different mid-wave infrared wavelengths 3.39, 4, and 5 μm. The difference between these three lenses was the length of the cylindrical subwavelength metaelements, with 0.9-, 4.0-, and 5.2-μm long cylindrical pillars available for characterization. These lenses were characterized by their optical scatter from different regions being interrogated by a laser beam much smaller than the overall width of the lens, which was a 1.5 or 3.5 mm beam along a 40 mm wide lens.

Overall, longer nano-pillars gave the best optical performance. Beam pass-through is lowest with the longest pillars, and highest with the shortest pillars. The intermediate-sized pillars (4-μm length) showed intermediate levels of beam pass-through with the exception at λ=3.39μm. The forward scattering lobe seen with this wafer at 3.39 μm was not seen with any other wafer or wavelength covered in this study. Excluding this exception, two patterns emerge in the beam pass-through study: beam pass-through is higher with shorter pillars and with longer wavelengths. This is most clearly seen with the wafer with 5.2-μm pillars at 3.39 μm wavelength at a beam location of +1 cm from the lens center, where only 0.03% of the total integrated scatter (TIS) is seen within the full-width half-maximum of the zeroth order lobe. At each increase in wavelength, the amount of beam pass-through increases for this wafer, with the largest increase coming in the change from 4- to 5-μm wavelength, which changes the beam pass-through from 1% to 43%. Additionally, the beam pass-through for the wafer with 0.9-μm pillars was high at the shortest wavelength of 3.39 μm with 28% of the TIS, but this too increased with every increase in wavelength, up to a

maximum of 79% when illuminated with the 5-μm beam. This behavior is largely unexpected, as the design post height and design wavelength were expected to give the best overall performance.

The resonance pattern seen with the wafer with the design nanopillar lengths of 4.0-μm at 3.39 μm incident wavelength is not seen with any other post height or wavelength. Therefore, it is recommended that tunable lasers be used to more finely test the spectral response of these metasurfaces. It is expected that the forward scattering lobe will disappear at a wavelength between 3.39 and 4 μm, simply because no forward scattering lobe was observed at 4 μm. Additionally, no forward scattering lobes were produced with the other wafers with nanopillar lengths of 0.9 and 5.2 μm at any wavelength. With a finer spectral resolution and a wider spectral range, there is potential to produce forward scattering lobes in these wafers as well. Finally, because the design post height was 3 μm, it is recommended that fabrication is redone in attempt to reach 3 μm post height. The closest available metasurface had post heights of 4.0 μm, which is far from ideal.

Bibliography

1. Yu, N. et. al. Light Propagation with Phase Discontinuities: Generalized Laws of Reflection and Refraction. Science 21 Oct 2011: Vol. 334, Issue 6054, pp. 333-337. DOI: 10.1126/science.1210713
2. A. V. Kildishev, A. Boltasseva, V. M. Shalaev, Planar photonics with metasurfaces. Science 339, 1232009 (2013). doi: 10.1126/ science.1232009; pmid: 23493714
3. N. Yu, F. Capasso, Flat optics with designer metasurfaces. Nat. Mater. 13, 139–150 (2014). doi: 10.1038/nmat3839; pmid: 24452357
4. P. Genevet, F. Capasso, F. Aieta, M. Khorasaninejad, R. Devlin, Recent advances in planar optics: From plasmonic to dielectric metasurfaces. Optica 4, 139–152 (2017). doi: 10.1364/OPTICA.4.000139
5. F. Falcone et al., Babinet principle applied to the design of metasurfaces and metamaterials. Phys. Rev. Lett. 93, 197401 (2004). doi: 10.1103/PhysRevLett.93.197401; pmid: 15600876
6. H. H. Hsiao, C. H. Chu, D. P. Tsai, Fundamentals and applications of metasurfaces. Small Methods 1, 1600064 (2017). doi: 10.1002/smtd.201600064
7. F. Aieta et al., Aberration-free ultrathin flat lenses and axicons at telecom wavelengths based on plasmonic metasurfaces. Nano Lett. 12, 4932–4936 (2012). doi: 10.1021/nl302516v; pmid: 22894542
8. L. Novotny, N. Van Hulst, Antennas for light. Nat. Photonics 5, 83–90 (2011). doi: 10.1038/nphoton.2010.237

9. Z. Sun, H. K. Kim, Refractive transmission of light and beam shapingwith metallic nano-optic lenses. Appl. Phys. Lett. 85, 642–644 (2004). doi: 10.1063/1.1776327
10. H. Shi et al., Beam manipulating by metallic nano-slits with variant widths. Opt. Express 13, 6815–6820 (2005). doi: 10.1364/OPEX.13.006815; pmid: 19498698
11. L. Verslegers et al., Planar lenses based on nanoscale slit arrays in a metallic film. Nano Lett. 9, 235–238 (2009). doi: 10.1021/nl802830y; pmid: 19053795
12. L. Yin et al., Subwavelength focusing and guiding of surface plasmons. Nano Lett. 5, 1399–1402 (2005). doi: 10.1021/ nl050723m; pmid: 16178246
13. Z. Liu et al., Focusing surface plasmons with a plasmonic lens. Nano Lett. 5, 1726–1729 (2005). doi: 10.1021/ nl051013j; pmid: 16159213
14. F. M. Huang, N. Zheludev, Y. Chen, F. Javier Garcia de Abajo, Focusing of light by a nanohole array. Appl. Phys. Lett. 90, 091119 (2007). doi: 10.1063/1.2710775
15. X. Ni, S. Ishii, A. V. Kildishev, V. M. Shalaev, Ultra-thin, planar, Babinet-inverted plasmonic metalenses. Light Sci. Appl. 2, e72 (2013). doi: 10.1038/lsa.2013.28
16. M. Kang, T. Feng, H.-T. Wang, J. Li, Wave front engineering from an array of thin aperture antennas. Opt. Express 20, 15882–15890 (2012). doi: 10.1364/OE.20.015882; pmid: 22772278
17. F. Monticone, N. M. Estakhri, A. Alù, Full control of nanoscale optical transmission with a composite metascreen. Phys. Rev. Lett. 110, 203903 (2013). doi: 10.1103/ PhysRevLett.110.203903; pmid: 25167411
18. Khorasaninejad et al., Metalenses: Versatile multifunctional photonic components. Science 358, eaam8100 (2017).

19. Bryan M. Adomanis, Matthew R. Miller, Stephen E. Nauyoks, Michael A. Marciniak, "Sensitivities of large-aperture plasmonic metasurface flat lenses in the long-wave infrared," Proc. SPIE 10542, High Contrast Metastructures VII, 1054210 (21 February 2018); doi: 10.1117/12.2291577

20. S. Jahani, Z. Jacob, All-dielectric metamaterials. Nat. Nanotechnol. 11, 23–36 (2016). doi: 10.1038/nnano.2015.304; pmid: 26740041

21. A. Arbabi, Y. Horie, A. J. Ball, M. Bagheri, A. Faraon, Subwavelength-thick lenses with high numerical apertures and large efficiency based on high-contrast transmitarrays. Nat. Commun. 6, 7069 (2015). doi: 10.1038/ncomms8069; pmid: 25947118

22. S. Vo et al., Sub-wavelength grating lenses with a twist. IEEE Photonics Technol. Lett. 26, 1375–1378 (2014). doi: 10.1109/ LPT.2014.2325947

23. Pko, 2006. 1: Cross-section of Buffon/Fresnel lens. 2: Cross-section of conventional plano-convex lens of equivalent power. [image] Available at: <https://en.wikipedia.org/wiki/Fresnel_lens#/media/File:Fresnel_lens.svg>.

24. Rama, 2005. First-order rotating catadioptric Fresnel lens, dated 1870, displayed at the Musée national de la Marine, Paris. [image] Available at: <https://en.wikipedia.org/wiki/Fresnel_lens#/media/File:MuseeMarine-phareFresnel-p1000466.jpg> .

25. Hecht, E. (2017). Optics. Pearson.

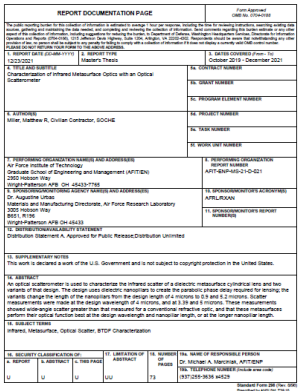

REPORT DOCUMENTATION PAGE

Form Approved OMB No. 0704-0188

The public reporting burden for this collection of information is estimated to average 1 hour per response, including the time for reviewing instructions, searching existing data sources, gathering and maintaining the data needed, and completing and reviewing the collection of information. Send comments regarding this burden estimate or any other aspect of this collection of information, including suggestions for reducing the burden, to Department of Defense, Washington Headquarters Services, Directorate for Information Operations and Reports (0704-0188), 1215 Jefferson Davis Highway, Suite 1204, Arlington, VA 22202-4302. Respondents should be aware that notwithstanding any other provision of law, no person shall be subject to any penalty for failing to comply with a collection of information if it does not display a currently valid OMB control number. PLEASE DO NOT RETURN YOUR FORM TO THE ABOVE ADDRESS.

1. REPORT DATE (DD-MM-YYYY)	2. REPORT TYPE	3. DATES COVERED (From - To)
12/23/2021	Master's Thesis	October 2019 - December 2021

4. TITLE AND SUBTITLE
Characterization of Infrared Metasurface Optics with an Optical Scatterometer

5a. CONTRACT NUMBER

5b. GRANT NUMBER

5c. PROGRAM ELEMENT NUMBER

6. AUTHOR(S)
Miller, Matthew R, Civilian Contractor, SOCHE

5d. PROJECT NUMBER

5e. TASK NUMBER

5f. WORK UNIT NUMBER

7. PERFORMING ORGANIZATION NAME(S) AND ADDRESS(S)
Air Force Institute of Technology
Graduate School of Engineering and Management (AFIT/ENI)
2950 Hobson Way
Wright-Patterson AFB OH 45433-7765

8. PERFORMING ORGANIZATION REPORT NUMBER
AFIT-ENP-MS-21-D-021

9. SPONSORING/MONITORING AGENCY NAME(S) AND ADDRESS(ES)
Dr. Augustine Urbas
Materials and Manufacturing Directorate, Air Force Research Laboratory
3005 Hobson Way
BldG1, R156
Wright-Patterson AFB OH 45433

10. SPONSOR/MONITOR'S ACRONYM(S)
AFRL/RXAN

11. SPONSOR/MONITOR'S REPORT NUMBER(S)

12. DISTRIBUTION/AVAILABILITY STATEMENT
Distribution Statement A. Approved for Public Release;Distribution Unlimited

13. SUPPLEMENTARY NOTES
This work is declared a work of the U.S. Government and is not subject to copyright protection in the United States.

14. ABSTRACT
An optical scatterometer is used to characterize the infrared scatter of a dielectric metasurface cylindrical lens and two variants of that design. The design uses dielectric nanopillars to create the parabolic phase delay required for lensing; the variants change the length of the nanopillars from the design length of 4 microns to 0.9 and 6.2 microns. Scatter measurements were made at the design wavelength of 4 microns, and at 3.39 and 5 microns. These measurements showed wide-angle scatter greater than that measured for a conventional refractive optic, and that these metasurfaces perform their optical function best at the design wavelength and nanopillar length, or at the longer nanopillar length.

15. SUBJECT TERMS
Infrared, Metasurface, Optical Scatter, BTDF Characterization

16. SECURITY CLASSIFICATION OF:			17. LIMITATION OF ABSTRACT	18. NUMBER OF PAGES	19a. NAME OF RESPONSIBLE PERSON
a. REPORT	b. ABSTRACT	c. THIS PAGE			Dr. Michael A. Marciniak, AFIT/ENP
					19b. TELEPHONE NUMBER (Include area code)
U	U	U	UU	73	(937) 255-3636 x4529

Standard Form 298 (Rev. 8/98)
Prescribed by ANSI Std. Z39.18